

Summer 2017

# A Low Cost Inflatable CubeSat Drag Brake Utilizing Sublimation

Adam Charles Horn  
*Old Dominion University*

Follow this and additional works at: [https://digitalcommons.odu.edu/mae\\_etds](https://digitalcommons.odu.edu/mae_etds)

 Part of the [Aerospace Engineering Commons](#), and the [Mechanical Engineering Commons](#)

---

## Recommended Citation

Horn, Adam C.. "A Low Cost Inflatable CubeSat Drag Brake Utilizing Sublimation" (2017). Master of Science (MS), thesis, Mechanical & Aerospace Engineering, Old Dominion University, DOI: 10.25777/1xaw-be17  
[https://digitalcommons.odu.edu/mae\\_etds/28](https://digitalcommons.odu.edu/mae_etds/28)

This Thesis is brought to you for free and open access by the Mechanical & Aerospace Engineering at ODU Digital Commons. It has been accepted for inclusion in Mechanical & Aerospace Engineering Theses & Dissertations by an authorized administrator of ODU Digital Commons. For more information, please contact [digitalcommons@odu.edu](mailto:digitalcommons@odu.edu).

**A LOW COST INFLATABLE CUBESAT DRAG BRAKE**

**UTILIZING SUBLIMATION**

by

Adam Charles Horn  
B.S. May 2015, Old Dominion University

A Thesis Submitted to the Faculty of  
Old Dominion University in Partial Fulfillment of the  
Requirements of the Degree of

**MASTER OF SCIENCE**

**AEROSPACE ENGINEERING**

**OLD DOMINION UNIVERSITY**

August 2017

Approved by:

Robert L. Ash (Director)

Brett Newman (Member)

Colin P. Britcher (Member)

## ABSTRACT

### A LOW COST INFLATABLE CUBESAT DRAG BRAKE UTILIZING SUBLIMATION

Adam Horn  
Old Dominion University, 2017  
Director: Dr. Robert L. Ash

The United Nations Inter-Agency Debris Coordination Committee has adopted a 25-year post-mission lifetime requirement for any satellite orbiting below 2000 km in order to mitigate the growing orbital debris threat. Low-cost CubeSats have become important satellite platforms with startling capabilities, but this guideline restricts them to altitudes below 600 km because they remain in orbit too long. In order to enable CubeSat deployments at higher release altitudes, a low-cost, ultra-reliable deorbit device is needed.

This thesis reports on efforts to develop a deployable and passively inflatable drag brake that can deorbit from higher orbital altitudes, thereby complying with the 25-year orbital lifetime guideline. On the basis of concepts first implemented during the NASA *Echo Satellite* Project, this study investigated the design of an inflatable CubeSat drag device that utilizes sublimating benzoic acid powder as the inflation propellant. Testing has focused on demonstrating the functionality of charging a Mylar drag brake bladder with appropriate quantities of benzoic acid powder, and the exposure to a controlled-temperature vacuum chamber causing the bladder to inflate. Although results show a measureable increase in internal pressure when introduced to anticipated orbital temperatures, a significant air-derived expansion prior to sublimation was encountered due to the undetectable volume of ambient residual air in the fabricated membrane bladders. These tests have demonstrated the feasibility of this approach, thereby demonstrating

that this concept can create a potentially smaller and less expensive drag device, eliminating inflation gas tanks and valves. In that way, this system can provide a low-cost, miniaturized system that reduces a CubeSat's orbital lifetime to less than 25 years, when placed at higher orbital altitude.

Copyright, 2017, by Adam Charles Horn, All Rights Reserved

## ACKNOWLEDGMENTS

First and foremost, I am very thankful for the overwhelming support and steadfastness of my advisor, Dr. Robert Ash. Dr. Ash not only provided guidance and encouragement for my studies and thesis, but he has also cultivated my passion for space systems engineering. Words cannot explain the immeasurable appreciation and gratitude to have such an influential mentor in my professional and personal life.

I would also like to thank:

- Dr. Brett Newman and Dr. Colin Britcher for providing their immense wealth of knowledge in my studies in the field of aerospace engineering and towards the completion of this thesis.
- Trevor Jackson and Joseph O'Connell for their support and accommodations at NASA Langley Research Center.
- Jeremy Peshl, Dr. Toza Popovic, Dr. Charles Sukenik, and Dr. Kenneth Brown for their advice and valuable input during the course of this thesis.

I am very thankful to work with such insightful professionals and for their support towards the success of this thesis.

## TABLE OF CONTENTS

	Page
LIST OF TABLES .....	viii
LIST OF FIGURES.....	ix
 Chapter	
I. INTRODUCTION.....	1
The Rise of Small Satellites .....	1
CubeSats.....	5
Orbital Space Debris .....	6
Orbital Lifetime Assessment.....	10
Drag Devices for CubeSats .....	14
Purpose.....	15
II. DRAG BRAKE DESIGN CONSIDERATIONS.....	17
NASA <i>Echo Satellite Project</i> .....	17
Previous Research .....	18
Atmospheric Considerations .....	19
Rigidization .....	26
III. INFLATION SYSTEM.....	29
Benzoic Acid Vapor Pressure Estimation .....	29
Sublimating Compound Quantity.....	33
Residual Air Expansion.....	34
IV. THERMAL MODEL .....	38
External Incident Radiation Sources .....	39
Orbital Mechanics .....	42

Thermal Environment.....	44
V. EXPERIMENTAL INVESTIGATIONS .....	50
Test Article Fabrication.....	50
Test Article Geometric Estimations .....	52
Differential Pressure Inflation Test .....	55
Thermal Vacuum Chamber Test .....	57
VI. RESULTS.....	61
Inflatable Internal Pressure – Volume Relationship.....	61
Simulated Environment Functionality.....	65
VII. DISCUSSION .....	75
VIII. CONCLUSIONS .....	79
Recommendations for Future Work.....	80
REFERENCES .....	81
APPENDIX A: SPACECRAFT’S POSITION VECTOR DETERMINATION .....	85
VITA .....	87

**LIST OF TABLES**

Table	Page
1. Benzoic Acid Properties .....	29
2. Drag Brake Material Properties .....	44
3. <i>Microsoft Kinect</i> Specifications .....	53
4. Test Article Characteristics .....	66
5. Air Inflatable Results .....	69

## LIST OF FIGURES

Figure	Page
1. Sputnik 1 <sup>1</sup> .....	1
2. Explorer 1 <sup>1</sup> .....	2
3. <i>SpaceWorks</i> Projection of Small Satellite Launches (1-50 kg) <sup>4</sup> .....	4
4. Number of Micro/Nano Satellite Launches from 2000-2016 <sup>4</sup> .....	5
5. 1U CubeSat <sup>6</sup> .....	6
6. Space Debris Distribution <sup>7</sup> .....	7
7. Altitude Distribution of Objects in Orbit around Earth <sup>8</sup> .....	8
8. STS-7 Windshield Damage from Orbital Debris <sup>8</sup> .....	9
9. Solar Flux F10.7 Index Behavior and Projection (10-22 Ws/m <sup>2</sup> ) <sup>12</sup> .....	12
10. Dimensionless Geomagnetic Index Ap Behavior and Projection <sup>12</sup> .....	12
11. Maximum Allowable Altitude as a Function of Ballistic Coefficient <sup>12</sup> .....	13
12. CanX-7 Drag Brake Concept <sup>13</sup> .....	14
13. GOLD Drag Brake Concept <sup>14</sup> .....	15
14. Fully-Inflated NASA Echo I Satellite <sup>15</sup> .....	17
15. Drag Brake Design Schematic .....	19
16. Variations in Nominal Atmospheric Properties .....	21
17. Profile of Circular Pillow-Shaped Geometry .....	22
18. Stress Formulations for Thin-Walled Pressure Vessel .....	24
19. Benzoic Acid Vapor Pressure Curve Comparison .....	32
20. Mass of Benzoic Acid Required to inflate a 1 m <sup>2</sup> Inflatable Drag Brake .....	34
21. Material Surface Roughness <sup>35</sup> .....	36

22. Volumetric Expansion of Minimum Inflatable Volume (1.3064 m <sup>3</sup> ) vs. Change in Ambient Pressure .....	37
23. Typical Spacecraft Thermal Environment .....	39
25. Approximate View Factors for Earth Reflected Solar Radiation Incident to a Sphere .....	41
26. Geometry of Orbital Elements .....	43
27. Earth Cylindrical Umbra from Parallel Solar Rays .....	44
28. Incident Heat Flux for a Spherical Mylar Drag Brake (H=1000km, i=0) .....	47
29. Thermal Response of Drag Brake at 1000 km Altitude for Various Orbital Inclinations .....	49
30. Air Removal Vacuum Setup .....	52
31. Depth-Disparity Model .....	55
32. Differential Pressure Test Setup .....	56
33. Cascade TEK High Vacuum Oven .....	58
34. Thermal Vacuum Test Setup .....	59
35. Thermal Vacuum Test Profile.....	60
36. Raw Point Cloud: 3.2 torr .....	62
37. Enhanced Point Cloud: 3.2 torr.....	62
38. Modified Point Cloud Ellipsoid Fit: 3.2 torr.....	63
39. Semi-Major and Semi-Minor Radius vs. Internal Pressure Approximation.....	64
40. Estimated Volume vs. Internal Pressure Approximation.....	65
41. Air Inflatable Surface.....	66
42. Benzoic Acid Inflatable Surface .....	66
43. Air Inflatable (12 torr) .....	67

	Page
44. Air Inflatable (7.1 torr) .....	68
45. Air Inflatable (5.1 torr) .....	68
46. Air Inflatable (2.9 torr) .....	68
47. Air Inflatable (2.4 torr) .....	69
48. Air Inflatable (0.5 torr) .....	69
49. Benzoic Acid Inflatable (20°C) .....	70
50. Benzoic Acid Inflatable (40°C) .....	71
51. Benzoic Acid Inflatable (60°C) .....	71
52. Benzoic Acid Inflatable (80°C) .....	71
53. Benzoic Acid Inflatable (100°C) .....	72
54. Benzoic Acid Inflatable (126.8°C) .....	72
55. Temperature History of Benzoic Acid Test Article .....	72
56. Ruptured Benzoic Acid Test Article Showing White Benzoic Acid Residue .....	73
57. Benzoic Acid Inflatable: Estimated Semi-Major/Semi Minor Radius vs Temperature .....	74
58. Benzoic Acid Inflatable: Estimated Volume vs. Temperature .....	74
59. Benzoic Acid Inflatable Condensed Powder .....	77
60. Benzoic Acid Inflatable Surface “Ribs” .....	78

## CHAPTER I

### INTRODUCTION

#### The Rise of Small Satellites

On October 4, 1957, the Soviet Union successfully launched the first artificial Earth satellite, *Sputnik 1*. Weighing only 83.5 kg and having a diameter of 58 cm, *Sputnik 1* spawned new political, military, technological and scientific developments which cultivated the next 60 years of space exploration (Figure 1).<sup>1</sup> The successful launch of *Sputnik 1* initiated rapid advancements in technology between the Soviet Union and the United States of America, also known as the *Space Age*.

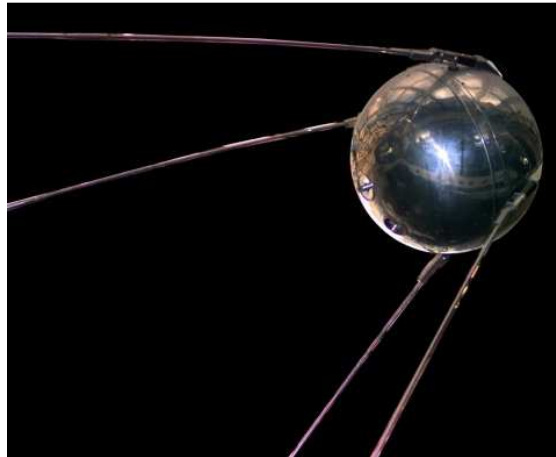


Figure 1. Sputnik 1<sup>1</sup>

Months after *Sputnik 1* was placed into orbit, the United States responded by successfully launching *Explorer 1* on January 31, 1958. Explorer 1 was the first satellite that the United States

placed in orbit, weighing 13.37 kg (Figure 2).<sup>1</sup> The success of the Sputnik and Explorer missions pioneered new technological innovations for space exploration and paved the way for spaceflight.

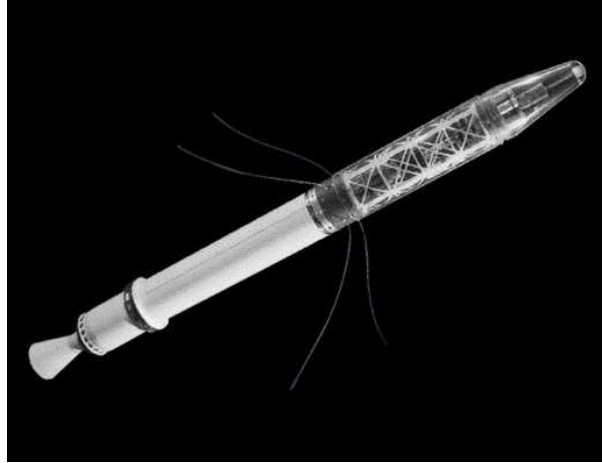


Figure 2. Explorer 1<sup>1</sup>

In the earlier years of spaceflight, the scientific payloads and satellites remained relatively small until advancements in launch vehicle capabilities made it possible to place larger payloads into orbit. Larger, more-sophisticated payloads were developed to meet the needs of more ambitious and challenging missions, where the on-going advancements in launch vehicle capabilities made it possible to continue these more-ambitious missions. These large, heavy spacecraft with fixed thrust profile seldom result in a perfect match with delivery system capabilities, necessitating the use of ballast masses to achieve the desired insertion orbit. The opportunity to substitute a small, secondary satellite payload for ballast mass was considered at first to be a novelty. However, in the past two decades there has been exponential growth in the

interest and use of much smaller satellites that can exploit the rapid miniaturization of a wide spectrum of digital devices and systems.

The gaining momentum of small satellites corresponds with lower orbital delivery costs and shorter time intervals between scientific data return and mission development and planning. Currently, the estimated cost of placing a payload into low Earth orbit is on the order of \$5,500 per kg, with minimum launch vehicle cost approaching \$75-million.<sup>2</sup> Small satellites are capable of using the excess capacity on a launch vehicle intended for a larger satellite deployment. The opportunity to “piggy-back” with primary satellites, delivered to prescribed orbits, can reduce orbital payload delivery costs dramatically.

Additionally, larger missions usually have considerable gaps between scientific data return and mission development and planning. For instance, mission development and planning for *Galileo* was initiated eight years prior to launch in October 1989. Small satellites allow the planning, development, and building phases to require between 18 and 24 months.<sup>3</sup> A short development time allows for targeted scientific goals that can be addressed rapidly in an affordable manner. Short development times and affordability results can allow consumers to consistently and frequently produce and launch new and improved variations that continuously expand science goals and objectives. These factors have helped ignite the explosive growth of small satellites and provide new opportunities for space exploration.

Since 1992, small satellites have been classified according to their mass, where satellites with a mass between 10 and 100 kg were considered microsattellites, and those with masses less than 10 kg were termed nanosatellites.<sup>5</sup> *SpaceWorks* has projected dramatic growth of small orbiting satellites in the 1 kg to 50 kg range, as shown in Figure 3.<sup>4</sup> With current rapid

advancements in technology, nanosatellites have experienced dramatic increases in scientific capabilities in the past decade. The evolution of micro/nanoelectronics, solar cell technology, battery technology and Micro-Electro-Mechanical Systems (MEMS) during the last decade has enabled miniaturized, cutting edge innovations for nanosatellites.<sup>5,6</sup> Because of these developments, the nanosatellite market has been highly favorable and is growing rapidly as demonstrated in Figure 4.<sup>4</sup>

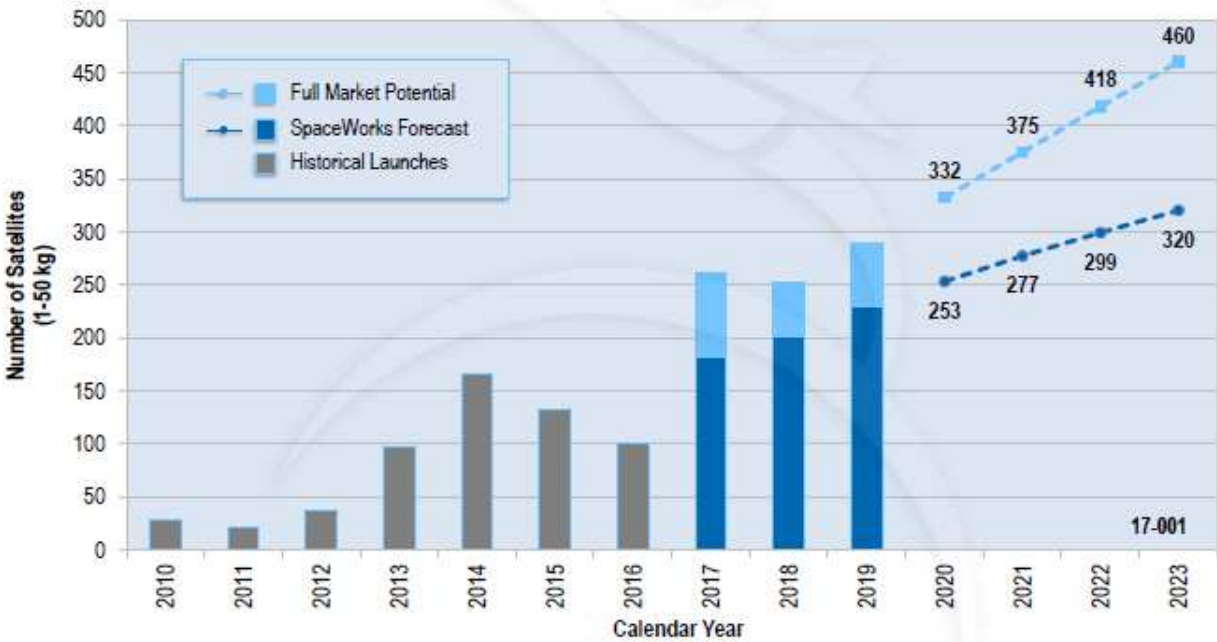


Figure 3. *SpaceWorks* Projection of Small Satellite Launches (1-50 kg)<sup>4</sup>

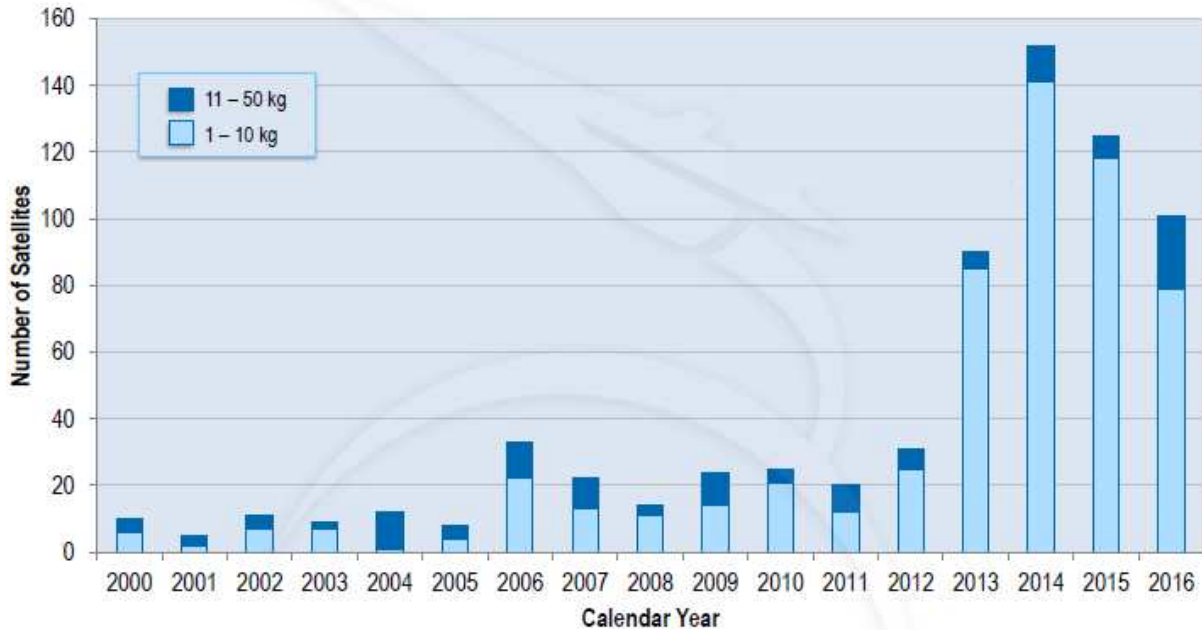


Figure 4. Number of Micro/Nano Satellite Launches from 2000-2016<sup>4</sup>

## CubeSats

CubeSats have been the dominant form of nanosatellites, classified in terms of 10x10x10 cm units called “U’s”(a 1U CubeSat is shown in Figure 5). The CubeSat was developed initially by California Polytechnic State University San Luis Obispo and Stanford University in 1999, serving as an educational tool for graduate students. The low-cost and short development times of CubeSats allow students to perform unique scientific research in space. For the past decade, the CubeSat platform has grown at an exponential rate, expanding to educational, military and commercial applications.

The simplicity of the CubeSat chassis and associated low-cost result typically from utilizing commercial, off-the-shelf components, standardized interfaces and standardized

picosatellite deployers.<sup>6</sup> The Poly-Picosatellite Orbital Deployer (P-POD) was designed to be integrated with launch vehicles as secondary payloads that integrate and enable deployment of CubeSats, thus avoiding the costs associated with dedicated launches. Additionally, their simplicity and cost efficiency allow for collaborative constellations of CubeSats that can be more versatile than larger satellites. However, deploying large numbers of these satellites over time can represent a potentially serious orbital debris hazard.

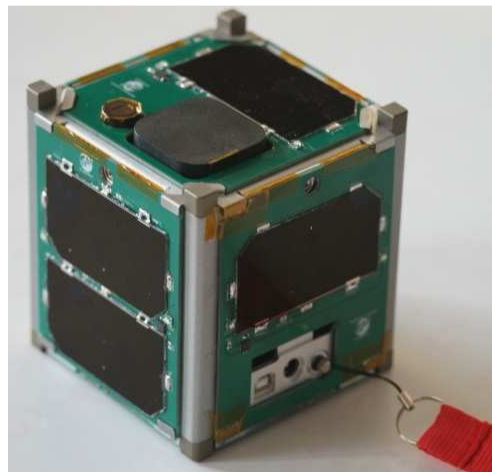


Figure 5. 1U CubeSat<sup>6</sup>

## **Orbital Space Debris**

Space debris is defined as any man-made object in orbit about the Earth which no longer serves a useful function, including nonfunctional spacecraft, spent launch vehicle stages, and fragmentation debris. More than 4,000 rocket launches have placed objects in an orbit around the Earth and these deployments have resulted in an increasingly dangerous accumulation of orbital

space debris. There are an estimated 700,000 orbiting objects with diameters between 1 and 10 cm and over 20,000 pieces with diameters greater than 10 cm in orbits between low Earth orbit and Geostationary altitudes.<sup>7</sup> Both Figures 6 and 7 illustrate the representation of the locations of non-functioning orbiting objects.<sup>7</sup> Figure 7 is the analogous logarithmic plot of the density distribution in orbit around Earth at various altitudes. Object density peaks correspond with the various orbital regimes (LEO, MEO, and GEO) indicating high risk collision potential for satellites traversing those regions.<sup>8</sup>

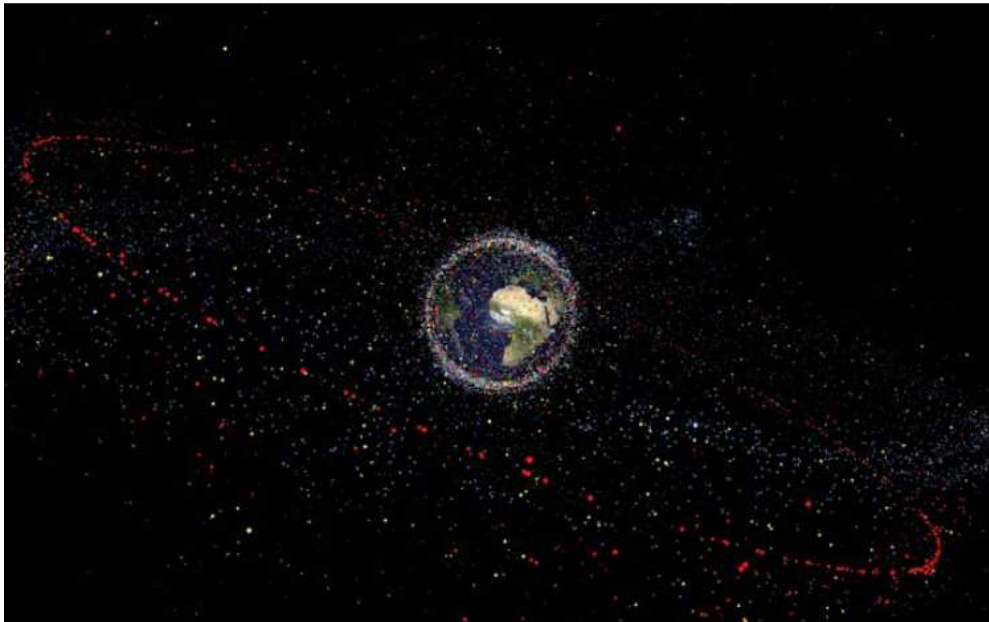


Figure 6. Space Debris Distribution<sup>7</sup>

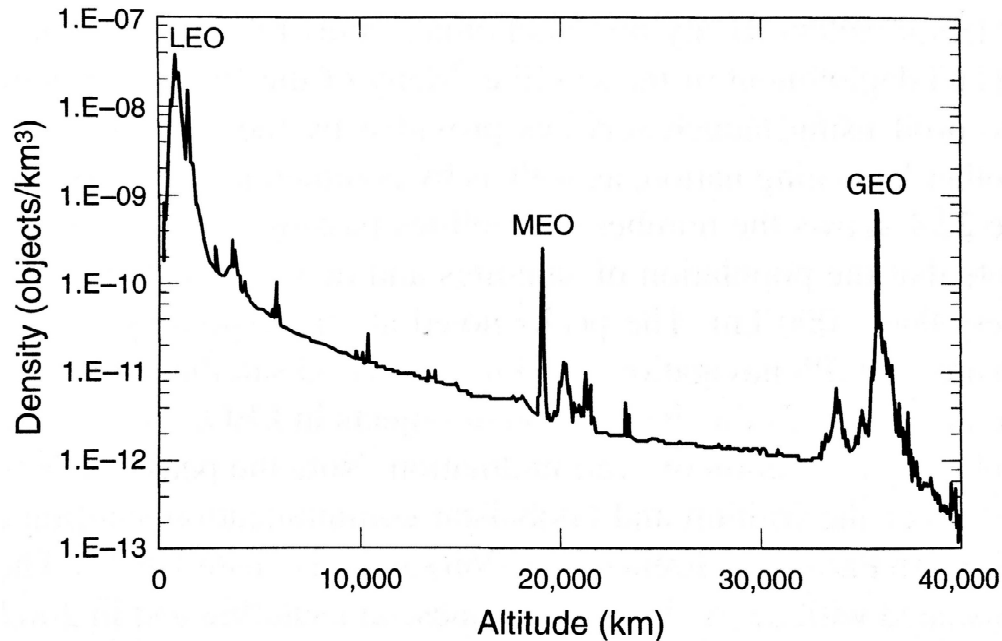


Figure 7. Altitude Distribution of Objects in Orbit around Earth<sup>8</sup>

Debris objects have orbital encounter speeds averaging around 11 km/sec, creating the possibility for catastrophic collisions with small orbital debris objects.<sup>9</sup> During the Space Shuttle Era, tiny paint flecks have caused observable damage to the space shuttle windows as the result of their high relative velocities. Damage to the windshield of STS-7 due to a 0.2 mm paint fleck impact is shown in Figure 8.<sup>9</sup> Not only does this pose a threat to astronauts and operational satellites and equipment but collisions in orbit will potentially generate more debris, leading to a debris cascade that could cripple space commerce.<sup>10</sup> The United States Department of Defense maintains a database of all objects in Earth orbit larger than 4 cm, to help functioning high-value orbital system managers anticipate and react to avoid possible collisions. An effective way of mitigating collision risk is to perform debris tracking and satellite-debris conjunction prediction,

but this process becomes progressively more difficult as the debris population increases and the number of orbiting CubeSats and other small satellites also dramatically increases.

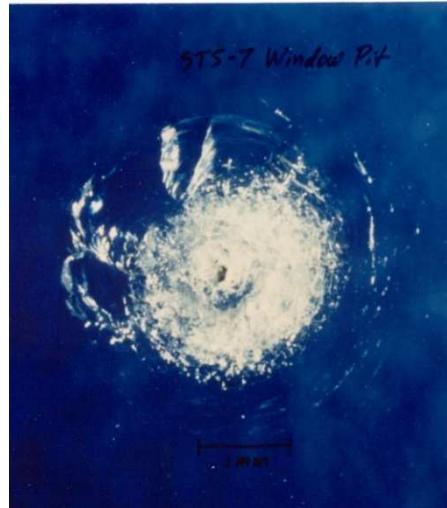


Figure 8. STS-7 Windshield Damage from Orbital Debris<sup>8</sup>

In an effort to limit and reduce the growing space debris hazard, mitigation policies and procedures have been established by the United Nations Inter-Agency Space Debris Coordination Committee (IADC). The IADC is an international governmental forum for the coordination of activities related to man-made and natural orbital debris.<sup>10</sup> The IADC Space Debris Mitigation Guideline for objects passing through LEO are as follows:

“A spacecraft or orbital stage should be left in an orbit in which, using accepted nominal projection for solar activity atmospheric drag will limit the orbital lifetime after completion of operations. A study of the effect of post-mission orbital lifetime limitation on collision rate and debris population growth has been performed by the IADC. This

IADC and some other studies and a number of existing national guidelines have found 25 years to be a reasonable and appropriate lifetime limit...”<sup>10</sup>

These mitigation guidelines can be problematic for CubeSats and other small satellites that piggy-back on larger primary spacecraft, where their operational orbit is dependent on the mission profile of the host payload. Because CubeSats typically lack adequate propulsion and maneuver capability, these satellites cannot perform or conduct controlled reentry or maneuvers for post mission disposal making them dependent on natural orbital decay if they are to comply with the IADC 25-year post-mission guideline. Other than restricting CubeSat deployments to orbits where estimated satellite lifetimes are shorter than 25 years, strategies which accelerate orbital degradation from higher orbital altitudes are needed.

### **Orbital Lifetime Assessment**

The orbital lifetime of a spacecraft must be estimated in order to verify compliance with the IADC 25-year post-mission lifetime requirement. Spacecraft orbital lifetime estimation requires: (1) specification of an atmospheric model; (2) an anticipated solar activity index; and (3) the ballistic coefficient of the spacecraft.

The ballistic coefficient of a spacecraft, denoted as  $\beta$ , is the primary factor controlling spacecraft orbital lifetime. The ballistic coefficient is defined as the ratio of the product of the spacecraft drag coefficient (typically estimated to be  $\sim 2.2$  for CubeSats) and the cross-sectional area in the direction of flight to the spacecraft mass.<sup>11</sup> Because the ballistic coefficient is dependent on the cross-sectional area of the spacecraft, this parameter provides the only practical means to influence the orbital decay rate, where

$$\beta = \frac{C_d A}{m} \quad (1)$$

The two other parameters that influence the decay time most commonly used in atmospheric models to represent solar emission state are solar activity F10.7 index and the geomagnetic Ap index. F10.7 measures the solar flux observed at a wavelength of 10.7 cm, and Ap is the measure of the response of Earth's magnetic field to solar activity.<sup>11</sup> Both of these quantities are highly dependent on current solar cycle. Historical data from previous solar cycles have been used to generate predictions for both F10.7 and Ap; however, there is currently limited ability to accurately estimate and forecast the variability of solar activity. Therefore, solar activity forecasts are tabulated employing 5, 50 and 95 percentile probabilities, providing a minimum, mean, and maximum prediction forecast.<sup>12</sup> Consequently, the low fidelity in being able to accurately forecast solar activity presents difficulty predicting orbital lifetimes. Figures 9 and 10 show the historical behavior and projection of the F10.7 index and Ap index, respectively in 5%, 50% and 95% solar activity predictions.<sup>12</sup>

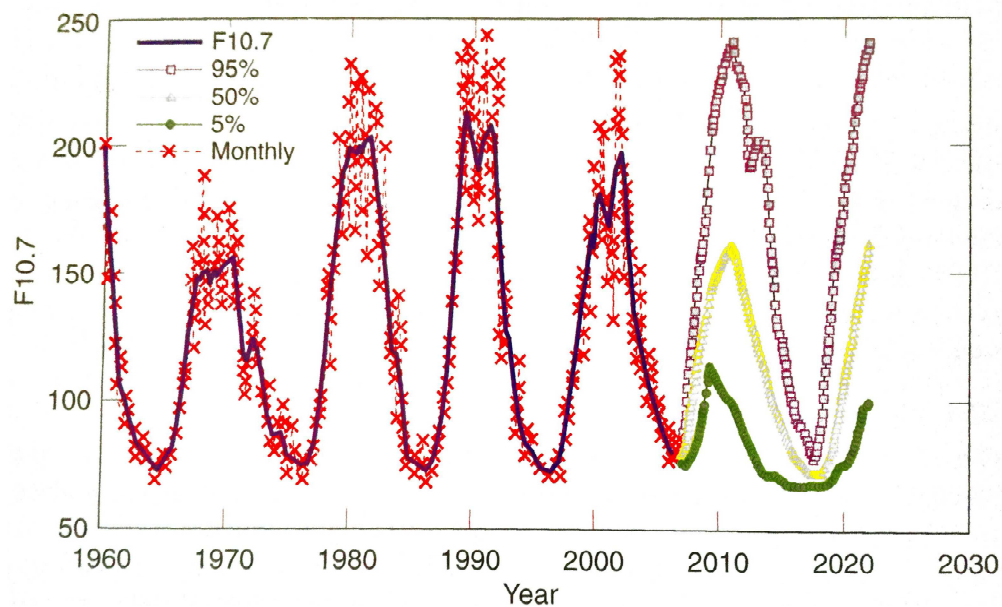


Figure 9. Solar Flux F10.7 Index Behavior and Projection (10-22 Ws/m<sup>2</sup>)<sup>12</sup>

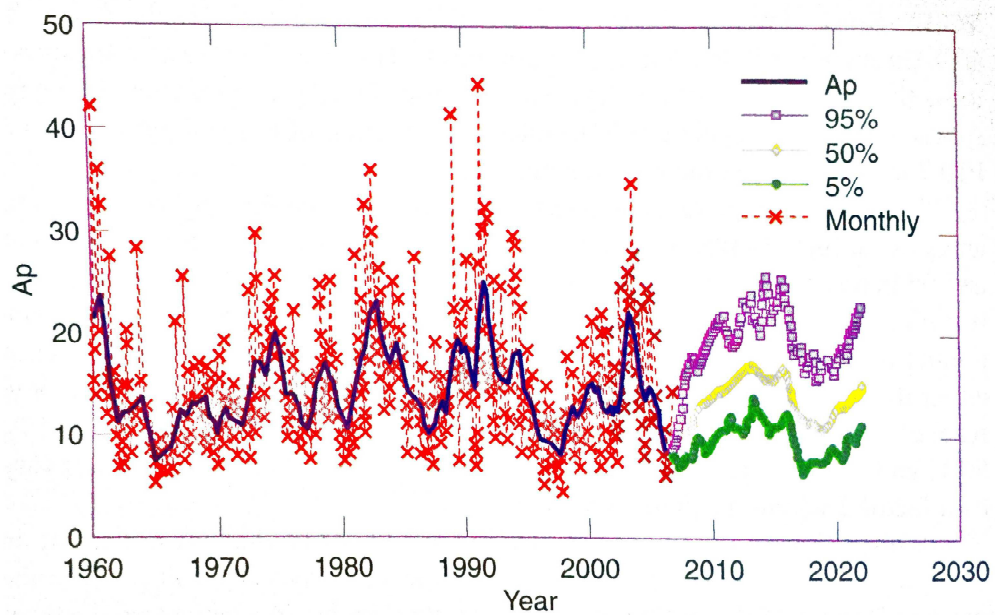


Figure 10. Dimensionless Geomagnetic Index Ap Behavior and Projection<sup>12</sup>

To represent the IDAC 25-year post-mission lifetime guideline, Figure 11 shows the maximum allowable altitude of a spacecraft as a function of the ballistic coefficient at various solar activity levels.<sup>12</sup> It can be seen that higher solar activity levels enable satellite deployments at higher maximum allowable altitude. However, the low fidelity in actually predicting the solar activity presents difficulty in specifying the circular orbital lifetime. Due to the uncertainty in atmospheric activity, CubeSat orbital deployment altitudes above 600 km do not guarantee compliance with IDAC orbital debris guidelines. Since typical CubeSats lack adequate propulsion and control, altering the ballistic coefficient can be an effective means of decreasing CubeSat orbital lifetime. This change can be done by increasing the cross-sectional area employing a drag enhancement device.

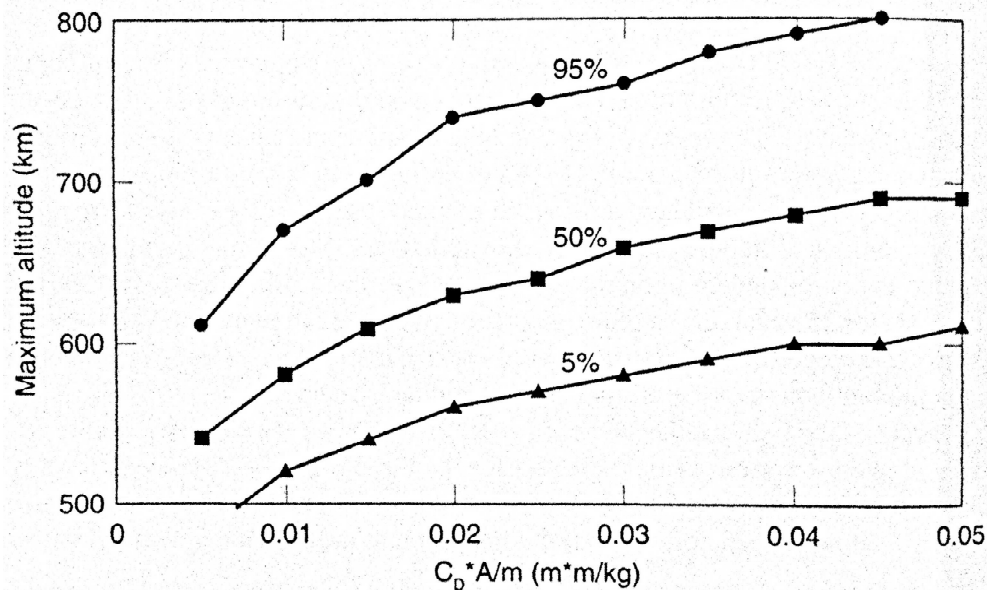


Figure 11. Maximum Allowable Altitude as a Function of Ballistic Coefficient<sup>12</sup>

## Drag Devices for CubeSats

Since deorbit systems are still in their infancy, there are few high Technology Readiness Level (TRL) devices guaranteed to satisfy the IADC 25- year guideline, including propulsive systems, solar and drag sails, balloons, and tethers.<sup>7</sup> These drag enhancement devices can be utilized on CubeSats/nanosatellites to effectively decrease the orbital lifetime and comply with orbital debris guidelines when placed at higher altitudes. Currently, there are several commercial, off-the-shelf drag devices available for CubeSats and other small satellites to enable the required control and maneuver to deorbit within the IADC 25-year postmission lifetime. *CanX-7* (Figure 12) is a passive deorbit drag sail developed at University of Toronto Institute for Aerospace Studies Space Flight Laboratory utilizing mechanically-deployed booms.<sup>13</sup> The purpose of *CanX-7* was to demonstrate a modular drag sail suitable for the CubeSat platform. With a similar objective, Global Aerospace has also developed an inflatable, spherical aerobrake, called *GOLD* that utilizes pressurized propellant canisters for inflation (Figure 13).<sup>14</sup>

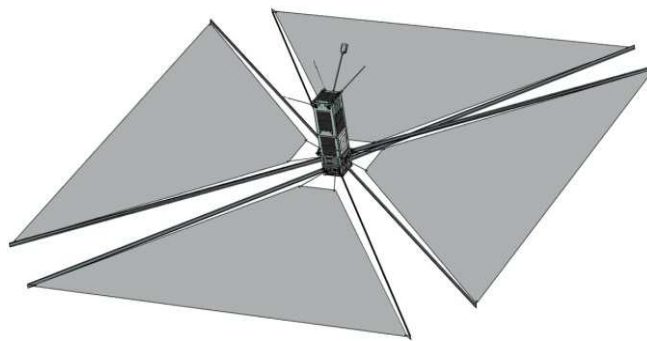


Figure 12. CanX-7 Drag Brake Concept<sup>13</sup>



Figure 13. GOLD Drag Brake Concept<sup>14</sup>

To date, both of these devices do not have flight heritage. Although these designs may provide an effective way of deorbit control, the current designs are rather complex and require a significant fraction of the available payload volume. There is a need for a smaller, simpler passive drag device design for utilization with small satellites/CubeSats.

### **Purpose**

In this thesis, a deployable and passively inflatable drag brake that can enable access to higher orbital altitudes while complying with the IADC 25-year post-mission lifetime guideline was investigated. Specifically, this thesis investigates the design of an inflatable CubeSat drag device that uses sublimating benzoic acid powder as the inflation propellant. The benzoic acid powder was employed previously in the NASA *Echo* satellite program in the 1960s. The use of a sublimating powder to inflate a drag brake for a small satellite has not been considered thus far, but this concept can create a potentially smaller and less expensive drag device.

On the basis of the NASA *Echo Project*, this thesis discusses the design considerations of a sublimating compound drag device for a CubeSat. A static inflation test and thermal vacuum chamber test have been conducted in order to demonstrate the feasibility of this approach, thereby demonstrating that this concept can create a potentially smaller and less-expensive drag device. In that way, this system can provide a low-cost, miniaturized system that reduces a CubeSat's orbital lifetime to less than 25 years, when placed at higher orbital altitude. In addition, this type of device can be released at some point, thereby enabling CubeSat systems to be stabilized or make orbital adjustments.

## CHAPTER II

### DRAG BRAKE DESIGN CONSIDERATIONS

#### *NASA Echo Satellite Project*

The present drag brake concept is based on the NASA *Echo Satellite* project.<sup>15,16</sup> The NASA *Echo Satellite* project demonstrated the feasibility of deploying, inflating and rigidizing a large space structure utilizing a sublimating propellant, thereby eliminating the need for pressurized gas tanks. The spherical *Echo* communication satellite shown in Figure 14 had a mass of 54.52 kg, and when fully-inflated, achieved a diameter of 30.5 m.<sup>15</sup> On August 12, 1960, *Echo I* was successfully launched, deployed and inflated to serve as the first passive communications satellite. At launch, the inflatable was packaged inside a 67.31 cm diameter container, from which the structure self-inflated to its full size in orbit.<sup>15</sup>

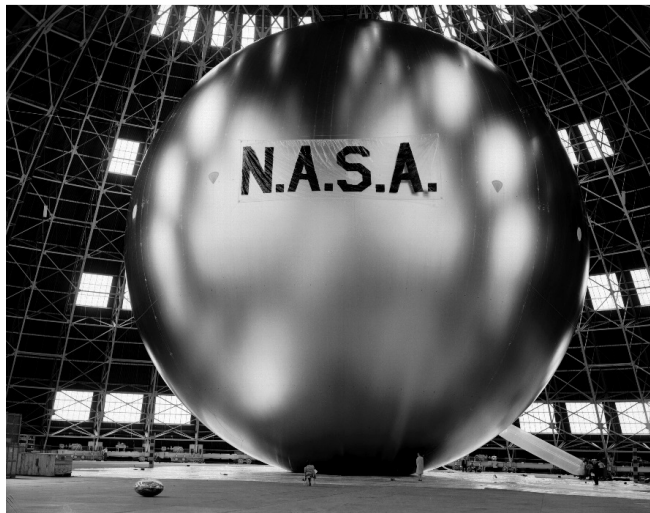


Figure 14. Fully-Inflated NASA Echo I Satellite<sup>15</sup>

The skin of the inflatable was made up of 12.7 micrometer-thick aluminized polyethylene terephthalate.<sup>15</sup> The surface was aluminized in order to achieve the required reflectivity, while shielding the polyethylene skin from ultraviolet radiation. In addition, it was discovered that the aluminized skin also provided a means for rigidizing the inflated structure via plastic deformation during inflation. That is, the internal pressures produced during in-orbit inflation exceeded the yield strength of the aluminum coating, causing it to deform plastically. As a result, even though it was expected that *Echo I* would be punctured by numerous micrometeorite impacts, the satellite retained its shape much longer than expected. The concepts and techniques that were utilized on the rather large *Echo* satellites can be scaled down to the smaller CubeSat platform to provide suitable deorbit capabilities. It is on that basis that the present drag design concept has been explored.

### **Previous Research**

Engineering students at Old Dominion University have investigated the feasibility of auto-inflating drag brake designs that can be integrated in CubeSat chassis. Previous graduate research and undergraduate design teams have demonstrated the miniaturization potential of these systems by assessing folding methods and deployment cavity designs.<sup>17,18</sup> It has been confirmed that a 1 m<sup>2</sup> uninflated bladder can be folded and placed inside a deployment cavity that occupies 25% of the overall 1-U CubeSat volume. Louku<sup>18</sup> focused on increasing the maximum circular-orbit altitudes from which CubeSats could be deployed, while complying with the pending 25-year maximum lifetime requirement. Additionally, Louku analyzed various inflatable geometries and inflatable materials and developed selection criteria.

Inflatable CubeSat drag brake designs consist of: (1) an inflatable structure, (2) the inflation system, (3) the deployment/release cavity, and (4) the anchoring/tether system. A schematic of the overall system can be seen in Figure 15. This thesis has focused on the inflatable structure and supporting vacuum experiments that validate the feasibility of this passive sublimating inflation system for CubeSats.

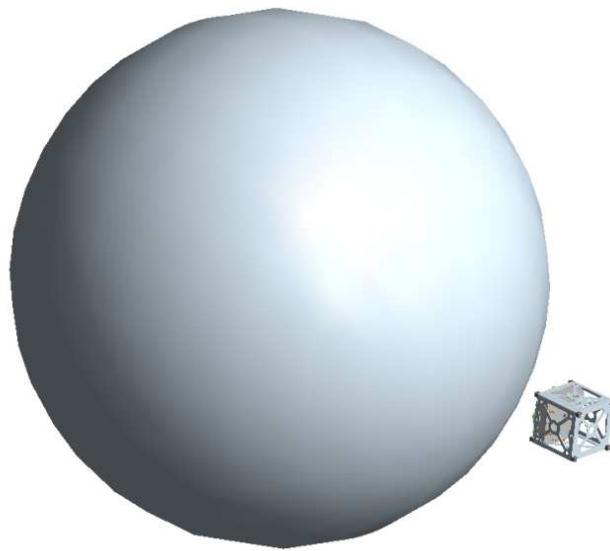


Figure 15. Drag Brake Design Schematic

### **Atmospheric Considerations**

The spacecraft operational environment is hostile due to the extreme vacuum, unfiltered ultraviolet solar radiation, and atomic oxygen erosion. At orbital altitudes, the relative concentrations of oxygen and other gases are quite different than their sea level concentrations, creating the potential for increased reactivity with spacecraft materials.

In order to establish design conditions, the nominal variation of atmospheric pressure, density, and mean-free-path with altitude are plotted in Figure 16, utilizing the *ARDC Model Atmosphere 1956*.<sup>19</sup> The ARDC model combines raw data from rocket flights and the rate of change of the orbital period of satellites to generate a database of atmospheric properties. It must be noted that the properties presented in this study are strictly average values, as they are functions of both time and position around Earth. However, the atmospheric properties presented in this model provide generalized values that are representative of those encountered at a given altitude.

Extremely low absolute pressures can cause premature inflation. Preliminary inflation tests of the *Echo* satellite showed that appreciable residual air remained inside the folds of the packaged inflatable and that air could result in an uncontrolled explosive deployment. The possibility of this rapid expansion of residual air when the canister equilibrated with the space environment could lead to rupture.<sup>16</sup> As a result, the Echo canister holding the packaged inflatable had to be evacuated to 1 torr prior to launch in order to limit the amount of residual air contained inside the folded satellite. Residual air has also been addressed in the development of an inflatable rigidizable iso-grid boom by ILC Dover Inc., under contract to the Jet Propulsion laboratory and NASA Langley Research Center.<sup>20</sup> During vacuum chamber tests, the planned two-minute deployment of the inflatable boom took less than 10 seconds due to an extremely small volume of residual atmosphere that remained in a pressure regulator and control valve line. The residual air inside of the CubeSat drag brake inflatable must be carefully managed to limit the possibility of a catastrophic expansion.

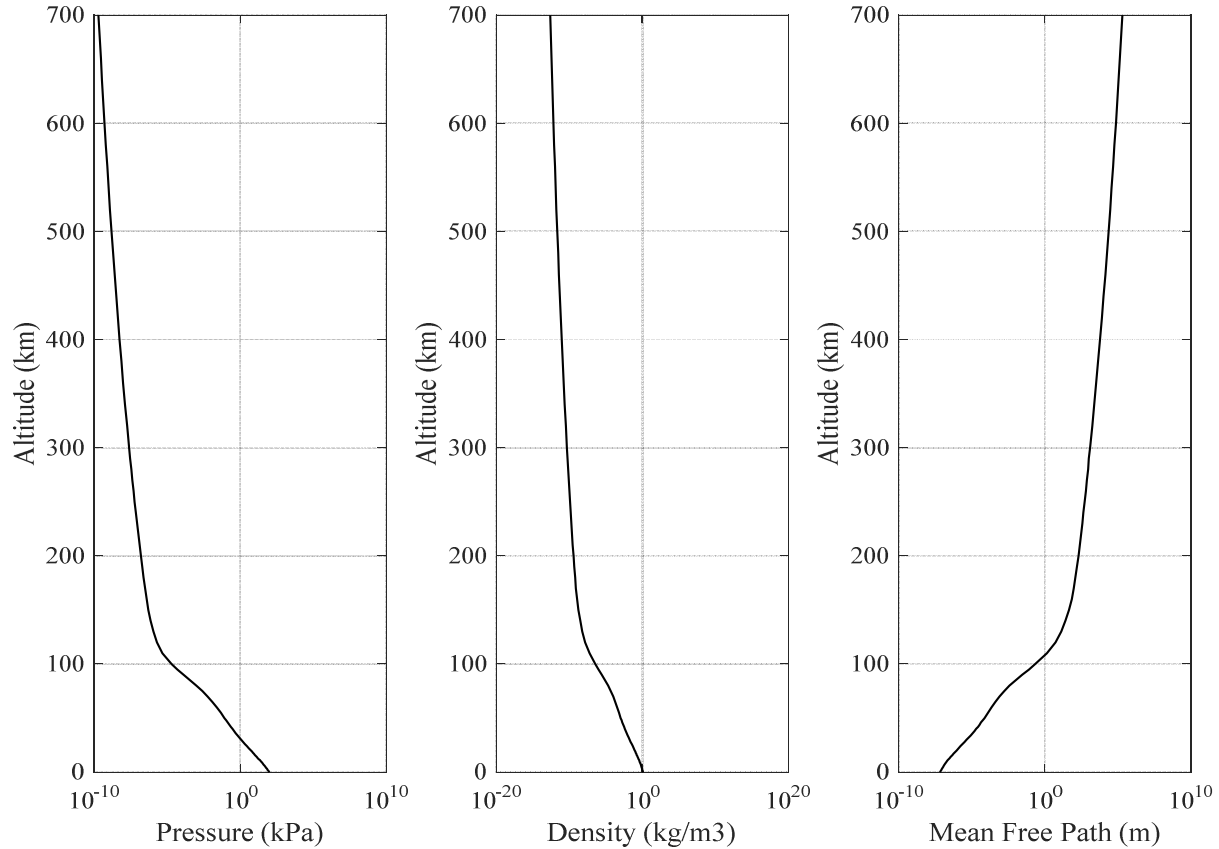


Figure 16. Variations in Nominal Atmospheric Properties

### Drag Brake Structure

A circular pillow-shaped drag brake geometry was utilized in this study, because of its simplicity. The nominal area of the uninflated bladder was  $1 \text{ m}^2$ . Additionally, polyethylene terephthalate (Mylar) has been employed as the skin of the drag brake structure. It is important to note that the present study could be enhanced by further consideration of other bladder materials as a possible way to achieve improved reliability in meeting the 25 year lifetime requirement.

Although the actual circular pillow-shaped geometry can be approximated as an oblate spheroid, an explicit parametrization of the inflated geometry in terms of elliptic functions was

developed by Mladenov and Oprea.<sup>21</sup> Their procedure is rather complicated. Basically, they defined a pair of dummy variables,  $u$  and  $v$ , from which they could map the three-dimensional surface ( $\mathbf{x} = x\mathbf{i} + y\mathbf{j} + z\mathbf{k}$ ) of the upper half of the balloon using:

$$\mathbf{x} = \mathbf{x}(u, v) = (x(u, v), y(u, v), z(u, v)) \quad (2)$$

$$x(u, v) = r \operatorname{cn}\left(u, \frac{1}{\sqrt{2}}\right) \cos v \quad (3)$$

$$y(u, v) = r \operatorname{cn}\left(u, \frac{1}{\sqrt{2}}\right) \sin v \quad (4)$$

$$z(u, v) = r \sqrt{2} \left[ E\left(\operatorname{sn}\left(u, \frac{1}{\sqrt{2}}\right), \frac{1}{\sqrt{2}}\right) - \frac{1}{2} F\left(\operatorname{sn}\left(u, \frac{1}{\sqrt{2}}\right), \frac{1}{\sqrt{2}}\right) \right] \quad (5)$$

where  $\operatorname{sn}(u, k)$  is the Jacobi sine function,  $\operatorname{cn}(u, k)$  is the Jacobi cosine function, and  $F(z, k)$  and  $E(z, k)$  are elliptic functions, defined in the paper. Figure 17 is a plot of the resulting parameterization functions.

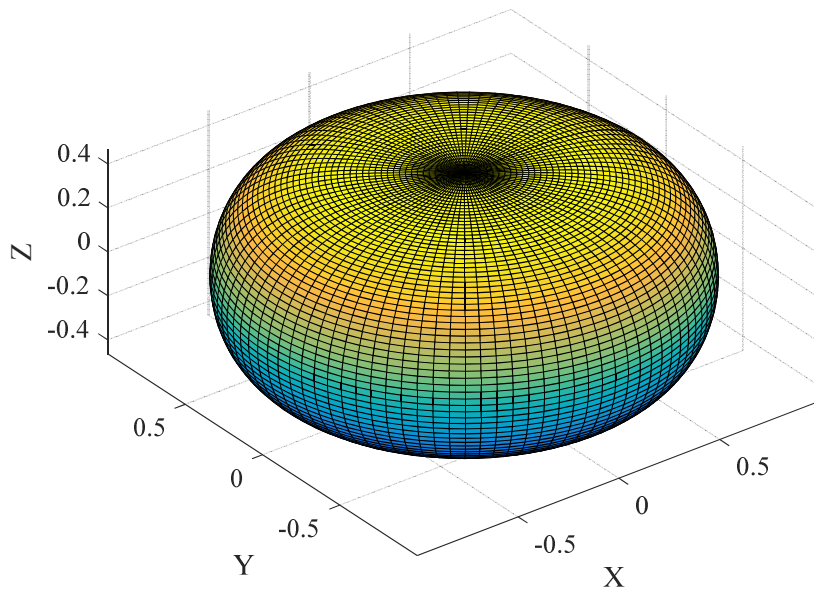


Figure 17. Profile of Circular Pillow-Shaped Geometry

Although the explicit parametrization in terms of elliptic functions are rather complex, the parametrization provides an effective tool for describing the unique geometric shape. Mladenov and Oprea manipulated the parametrization expressions to provide relationships for the radius, thickness and volume of the inflated structure. The deflated radius,  $a$ , can be related approximately to the inflated radius,  $r$ , while the corresponding height (thickness),  $\tau$ , and volume,  $V$ , can be approximated.<sup>21</sup>

$$a \approx 1.3110r \quad (6)$$

$$\tau \approx 1.1981r \quad (7)$$

$$V \approx 2.7485r^3 \quad (8)$$

The drag brake structure was treated as a membrane shell of revolution. This assumption is justified because the ratio of the wall (membrane) thickness to the inflated radius is much smaller than unity ( $t/R \ll 1$ ). Therefore, the structure acts as a membrane and bending stresses are negligibly small. On this basis, the meridian is defined as the axis of rotation, and the circumference is defined as the line intersected by the wall and the axis of rotation, perpendicular to the meridian. For uniform internal pressure, the meridional stress,  $\sigma_1$ , acts parallel to the meridian and a circumferential stress, or hoop stress,  $\sigma_2$ , acts parallel to the circumference. Employing the thin-walled pressure vessel model,  $\sigma_1$  and  $\sigma_2$  were assumed to be uniform throughout the thickness of the membrane. Expressions for  $\sigma_1$  and  $\sigma_2$ , for a membrane of revolution are displayed in Figure 18.<sup>22</sup>

$$\sigma_1 = \frac{qR_2}{2t} \quad (9)$$

$$\sigma_2 = \frac{qR_2}{2t} \left( 2 - \frac{R_2}{R_1} \right) \quad (10)$$

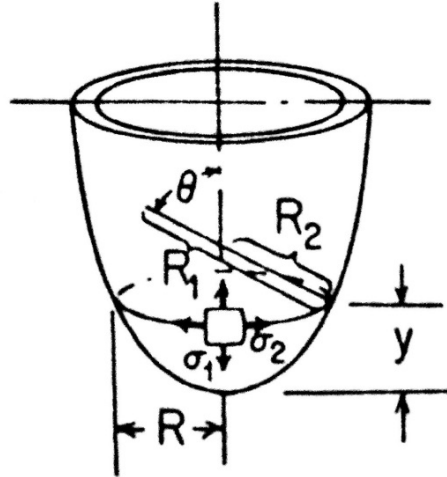


Figure 18. Stress Formulations for Thin-Walled Pressure Vessel

Drag forces acting on CubeSat drag brake systems are still characterized utilizing:

$$F_D = ma = \frac{1}{2} \rho S C_D V_r^2 \quad (11)$$

However, in order to understand the drag forces acting on the drag brake, the atmospheric density and the mean free path must be considered. The mean free path is the average distance between particle collisions. At sea level, the mean free path is ~68 nanometers. The nominal mean free path variation with altitude, based on the 1956 *ARDC Model Atmosphere*, was plotted in Figure 16. The mean free path provides critical information on the type of flow regime, utilizing the Knudsen number, Kn, which is defined as the ratio of the mean free path to a characteristic geometrical length dimension. Continuum flow is considered when Kn is less than 0.2. Transitional flow is noted when Kn is between 0.01 and 1, while flows are considered to be rarefied when the Knudsen is greater than 1.<sup>23</sup> Due to the large mean free paths at orbital altitudes of interest, the aerodynamic drag cannot be determined in a continuum model. The flow is sufficiently rarefied to be modeled as a free molecular flow in which the drag forces

acting on the spacecraft depend on gas-surface interactions, in addition to simple collisional rebound interactions.

These gas-surface interactions create small drag forces acting on a spacecraft at orbital altitudes. Usually, spacecraft mass, velocity, and the cross-sectional area can be estimated with negligible error. However, the density and the drag coefficient are large sources of uncertainty.

In Chapter 1, the challenges of accurately estimating, much less forecasting, local variations in atmospheric density were discussed. Obviously, that creates a level of uncertainty in empirical atmospheric models. Additionally, most empirical atmospheric models assume the drag coefficient of all satellites to be 2.2. This may provide a simplified estimate of the drag force, but the actual drag also depends on atmospheric density and the actual orientation of the satellite travelling along its line-of-flight. Actual atmospheric composition and temperature along with the surface adsorption and reaction behavior of molecules impinging on the surface produce dynamic variations in drag coefficient that can vary widely from the 2.2 assumption. Without a reliable estimation of the true satellite drag coefficient, forward propagation forecasts of satellites in low Earth orbit become inaccurate.

Estimation of satellite drag coefficient is a strong function of the gas-surface, gas composition, atmospheric and surface temperature, relative velocity and the amount of energy which oncoming molecules lose when they collide with spacecraft surfaces.<sup>24</sup> The gas-surface collisions are characterized typically utilizing an *accommodation coefficient* factor. The accommodation coefficient provides an approximation of how the kinetic energy of a molecule should be adjusted due to the thermal energy liberated at the surface. If  $E_i$  is the kinetic energy of the incident molecule, and  $E_r$  is the kinetic energy of the re-emitted molecule, while  $E_w$  is the

kinetic energy that the reemitted molecule would have if it left at the surface temperature of the spacecraft, the accommodation coefficient,  $\alpha$ , is defined.<sup>24</sup>

$$\alpha = \frac{E_i - E_r}{E_i - E_w} \quad (12)$$

In low Earth orbit, the abundance of atomic oxygen molecules can heavily contaminate the surface of a spacecraft with absorbed molecules resulting from collisions. These heavily-coated surfaces (with absorbed molecules) result subsequently in the incident molecules being re-emitted in a more or less diffuse manner, losing a large portion of their kinetic energy.<sup>25</sup> Therefore, the absorbed molecules increase the energy accommodation and broaden the angular distribution of molecules re-emitted from the surface.

Direct Simulation Monte Carlo (DSMC) methods can be employed to improve the estimation accuracy of the actual drag forces.<sup>25</sup> DSMC employs velocity distribution functions to represent a large number of actual molecules; then continuously solves the Boltzmann equation in a time-accurate and naturally unsteady manner. This method utilizes time step sizes smaller than the mean collision time interval where the motion can be decoupled from periods of collision between multiple molecules or between a molecule and a surface. These simulations are computationally intensive due to their statistical approach, but DSMC should be considered in future work in determining more accurate estimations of drag coefficient.

### **Rigidization**

Once inflated, these drag brake structures must retain structural rigidity in order to maintain their shape once internal pressure is lost due numerous unavoidable micro-meteor impacts and material degradation. Several rigidization techniques have been proposed, involving

both chemical and mechanical means, including resins that set when exposed to ultraviolet (solar) radiation, thermosetting resins, glass transition resins, and metal laminates.<sup>26,27</sup> *Echo I* employed a second, slower sublimating powder, in conjunction with the primary benzoic acid powder, in order to generate a more-sustainable but lower vapor pressure and extend the satellite lifetime by several weeks.<sup>15</sup> General considerations in determining an effective rigidization process include: methods of pre-inflation stowage and handling, inflation energy requirements, and structural performance.

The United States Air Force has conducted preliminary research on the performance of ultraviolet (UV) setting resins, relying on environmental UV radiation for curing and hardening space structures.<sup>26</sup> Utilizing solar UV radiation results in an entirely passive rigidization process while integrated UV lamps have also been demonstrated. It is important to note that the use of environmental radiation can result in an uneven cure process that can result in warping. Additionally, consideration must be given to the rigidizable skin to ensure sufficient UV transmission for curing. Also, this technique is irreversible and the storage environment must be controlled.

UV setting resins, and thermosetting resins are particularly attractive due to their high stiffness and strength for terrestrial applications.<sup>26</sup> Thermally cured composites can rely on the sun or a local source of heat for curing, resulting in a passive or a highly controlled rigidization process.<sup>26</sup> This process is also irreversible and the storage and packing environment must be controlled. Additionally, cure energy requirements can be significant and there may be difficulty in ensuring a uniform cure.

Glass transition rigidization, or sub-T<sub>g</sub> rigidization, utilizes the glass transition temperature range of various materials. Thermosetting polymers have a glass transition temperature range where the polymer transitions from being hard and rigid to a “glassy” and more pliable state.<sup>27</sup> When a polymer is exposed to its glass transition temperature range, it causes the mobility of the polymer molecules to significantly increase, and once cooled, the polymer returns to its hardened, rigid state. The skin of an inflatable structure can employ thermosetting polymers to create a self-rigidizing structure below the glass transition temperature range. In order to be effective, low power heating and controlled thermal environmental requirements are needed to ensure that the glass transition temperature is reached, but once deployed, passive rigidization occurs as the inflatable cools.

Stretched metal laminates have space heritage in several missions, including Echo II and Explorer XIX.<sup>28</sup> Typically, metal laminates contain thin layers of aluminum, or some other ductile metal, bonded to thin layers of polymers. This layered skin allows for the inflation pressure of the structure to exceed the yield strength of the metal, plastically deforming the metal to provide increased stiffness. The extensive use of metal laminates has resulted because of their simplicity in manufacturing and handling, along with their predictable rigidization, and low outgassing behavior. Even then, careful control of the inflation gas pressure must be assured in order to avoid potential rupture, since higher pressures will exceed the desired yield stress condition for the particular metal.

Overall, the inflatable must be rigidized to provide long-term structural performance. This needs to be considered in future work in order to achieve an acceptable technique for maintaining structural rigidity of the drag brake.

## CHAPTER III

### INFLATION SYSTEM

Sublimating benzoic acid powder was considered as the primary inflation agent for the drag brake design. At room temperature and pressure, benzoic acid is a colorless, crystalline solid and is used commonly in food preservatives and in the pharmaceutical industry.<sup>29</sup> The vapor pressure behavior of benzoic acid can be exploited to sustain internal pressures that are sufficient to inflate space structures, similarly for the NASA *Echo Satellites*. On that basis, accurately characterizing the vapor pressure behavior of pharmaceutical grade benzoic acid powder over anticipated orbital equilibrium temperatures will be the primary design basis for inflation of the drag brake. Relevant properties of benzoic acid are summarized in Table 1.<sup>30</sup>

Table 1. Benzoic Acid Properties

<b>Chemical Formula</b>	$C_7H_6O_2$
<b>Molar Mass</b>	$122.12 \text{ g}\cdot\text{mol}^{-1}$
<b>Density</b>	$1.2659 \text{ g}\cdot\text{cm}^{-3}$ at 15 °C
<b>Triple Point Temperature</b>	122.37 °C
<b>Ambient Vapor Pressure</b>	0.0933 Pa at 25 °C
<b>Latent Heat of Sublimation</b>	$90. \text{ kJ}\cdot\text{mol}^{-1}$

#### Benzoic Acid Vapor Pressure Estimation

The dynamic process experienced by a deflated bladder, when exposed to a space-like environment resulting from internal sublimation of benzoic acid particles, has never been

documented. If experiments are to be repeatable, an accurate characterization of the phase behavior of benzoic acid vapor is required.

As is the case for many substances, the solid-vapor phase equilibrium curve for benzoic acid at temperatures below the triple point (122.37°C) involves pressures substantially lower than one atmosphere. While the low-pressure behavior of sublimating benzoic acid is not tabulated in any known reference documents, the gas phase at these moderate temperatures and low pressures should closely approximate ideal gas behavior. An ideal gas model has been examined, along with a more-empirical but more accurate model that is employed by the National Institute of Standards and Technology.

The Clausius-Clapeyron equation is often used to estimate vapor pressures of pure solids at low absolute pressures and can provide accurate estimation of vapor pressure variation with temperature.<sup>31</sup> This equation provides reliable vapor pressure estimations when: (1) assuming the specific volume of the solid phase is negligible when compared with the specific volume of the vapor phase, (2) the change in volume that accompanies sublimation can be approximated as the volume of vapor, (3) the enthalpy of sublimation is independent over the temperature range of interest, (4) the pressures are so low that the gas phase molecules behave like an ideal gas and the resulting vapor can be considered to be an ideal gas.<sup>32</sup> With these approximations, the saturation pressure and some thermodynamic state ( $P_2, T_2$ ), can be related to a known reference state ( $P_1, T_1$ ), according to:

$$\ln\left(\frac{P_1}{P_2}\right) = \frac{\Delta H_{sub}}{R} \left(\frac{1}{T_2} - \frac{1}{T_1}\right) \quad (13)$$

The Clausius-Clapeyron expression provides an exponential relation between absolute pressure and temperature. Additionally, the estimated vapor pressure is highly dependent on the latent heat of sublimation,  $\Delta H_{sub}$ , also called the *enthalpy of sublimation*. The enthalpy of sublimation is the thermal energy required to change one mole of a substance from its solid phase to its vapor phase at a fixed temperature and pressure. Consequently, large values of the latent heat of sublimation translate to increased thermal energy requirements to effect vapor pressure phase change.

The Clausius-Clapeyron equation assumptions are reasonable at low pressures and temperatures. However, at the higher pressures associated with liquid-vapor phase transitions, and near the critical point, the vapor phase does not approximate an ideal gas, and the Clausius-Clapeyron model is inappropriate. In the higher temperature and pressure regime, the Antoine equation can be used for estimating vapor pressures.<sup>33</sup>

The Antoine equation is an empirical, but more accurate, way to estimate solid-vapor equilibrium pressures when the ideal gas assumption is inaccurate. The Antoine equation was empirically derived employing thermogravimetry, correlating the rate of mass loss per unit area of substance with vapor pressure over a specific temperature range.<sup>33</sup>

$$\log_{10} P = A - \left( \frac{B}{T + C} \right) \quad (14)$$

Although restricted to specific temperature ranges represents a limitation, employing the Antoine equation and the substance-specific Antoine parameters over the specified range, produces a more reliable vapor pressure estimate at higher pressures and temperatures. Figure 19 illustrates the estimated solid-vapor phase equilibrium curve for benzoic acid between 0 and 150°C for, including both Clausius-Clapeyron and the Antoine formulations. Because the ideal

gas law assumption is valid at lower pressures, the Clausius-Clapyron equation can be used below the empirically formulated temperature range of the Antoine equation. As temperature increases, the Antoine equation will become a more accurate representation of the solid-vapor phase equilibrium curve due to the increased vapor pressures.

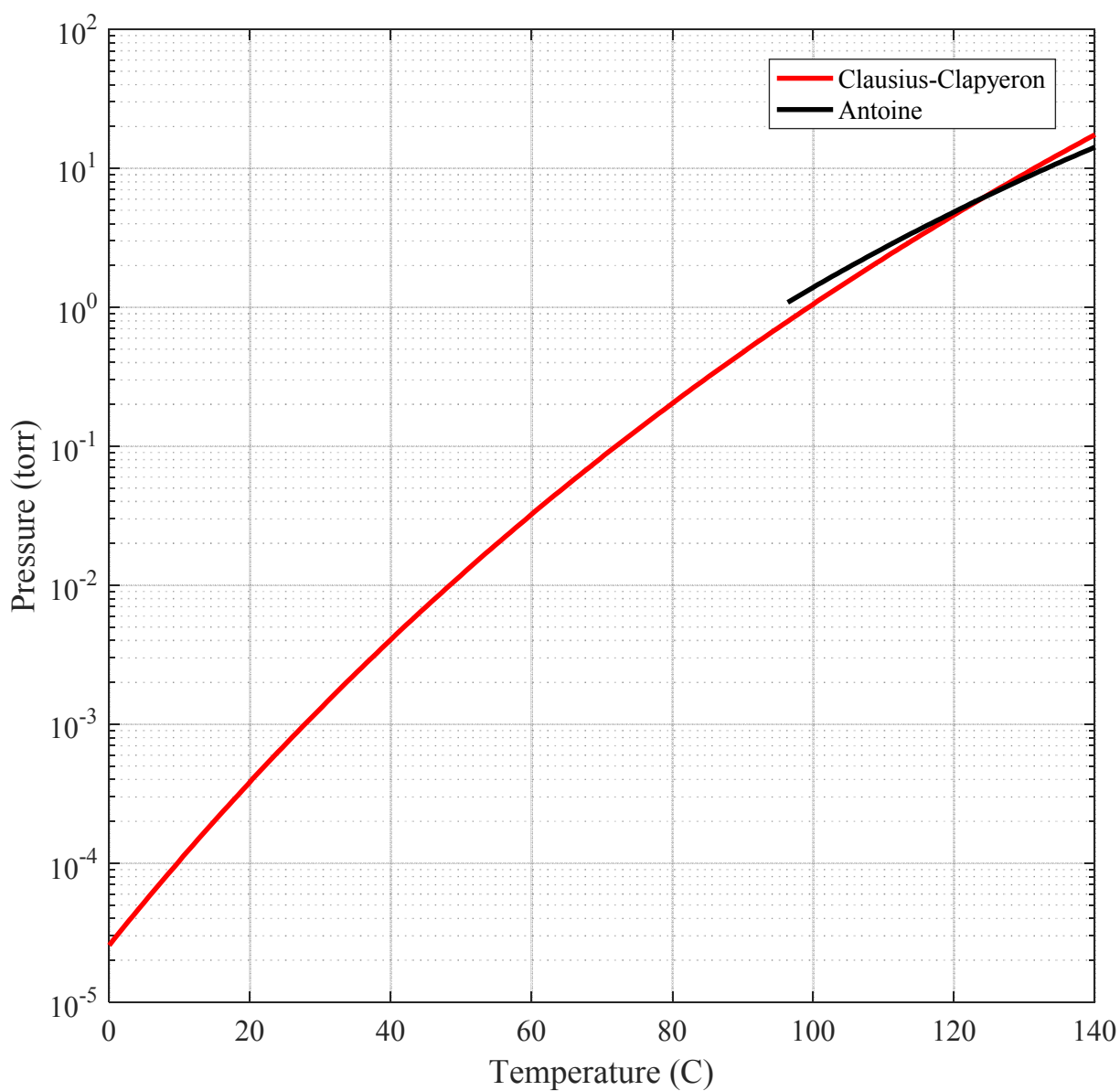


Figure 19. Benzoic Acid Vapor Pressure Curve Comparison

### Sublimating Compound Quantity

To determine the necessary quantity of sublimating compound “propellant” needed to effectively achieve the desired inflation pressure as characterized in Figure 19, benzoic acid vapor can be characterized as an ideal gas, i.e.

$$PV = nRT \quad (15)$$

Assuming that all benzoic acid powder is converted to vapor, the ideal gas law can be used to estimate number of moles required to achieve a desired solid-vapor equilibrium condition. Therefore, controlling the amount of sublimating compound present inside the inflatable allows for the control of the internal pressure of the inflatable.

As a reference case for this thesis, a circular pillow-shaped drag brake with an uninflated cross sectional area of  $1 \text{ m}^2$ , has been assumed. That drag brake should achieve a fully inflated volume of  $0.496 \text{ m}^3$ . Employing a molecular weight of 122.12, the required mass of benzoic acid powder needed to achieve the equilibrium solid-vapor inflation condition corresponding to the saturation temperature, yields a linear relationship, as shown in Figure 20.

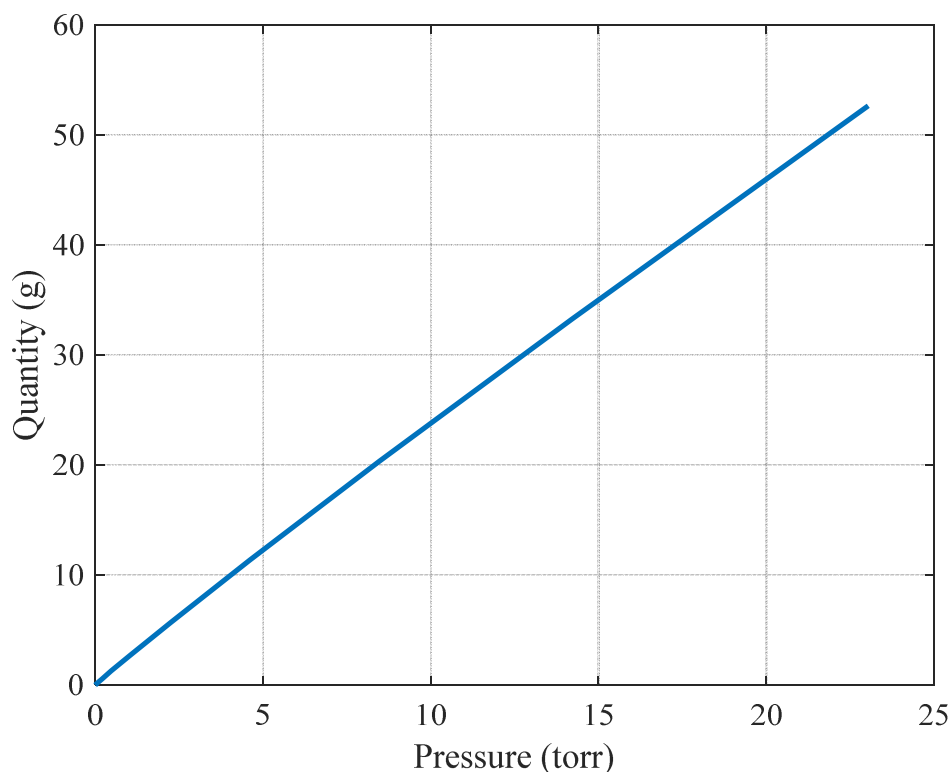


Figure 20. Mass of Benzoic Acid Required to inflate a 1 m<sup>2</sup> Inflatable Drag Brake

### **Residual Air Expansion**

Since it is not possible to manufacture a sealed membrane incorporating benzoic acid powder under ambient conditions, without incorporating excessive residual air, those influences must be examined. Expansion of residual air can be substantial since the occupied air volume can increase nearly 1000-fold when the ambient pressure is reduced to 1 torr. The cavity holding the drag brake prior to deployment will be exposed to the external environment; as a result, auto-inflation can occur without sublimation if sufficient residual air is present during the spacecraft ascent. Furthermore, depending on how the deflated structure is exposed to the local environment, a potentially-destructive inflation rupture could result from excessive air.

Preliminary tests of the Echo Satellites showed that such destructive processes were possible because air left inside of the folds of the packaged satellite could drive catastrophic expansion.<sup>16</sup>

In the present case, control and characterization of residual air effects required careful documentation. The actual mass of residual air left in the bladder during fabrication is extremely difficult if not impossible to measure. Consequently, the mass of residual air that can be tolerated inside of the inflatable was an important consideration. The volume that can be occupied by that same quantity of air, when the external pressure corresponds to ambient orbital pressure conditions, can exceed the available inflated volume, potentially capable of producing a rapid and destructive inflation condition.

At low pressures, the residual air in the inflatable can be modeled as an ideal gas. Therefore, if the temperature and air mass are assumed to be constant, the pressure and volume corresponding to two different testing states can be equated to estimate the actual residual air mass. Also known as Boyle's Law, the pressure exerted by an ideal gas is inversely proportional to the occupied volume.<sup>34</sup>

$$P_1V_1 = P_2V_2 \quad (16)$$

The actual minimum volume occupied by residual air during manufacture can only be estimated. An effort was made to estimate the minimum occupied residual air volume based on an assumed surface roughness characterizing the Mylar skin material. The surface roughness of a material is the property of surface texture resulting from uneven topography of the surface. Illustrated in Figure 21, there are several parameters that can be employed to represent the irregularities in the materials surface including the Root Mean Square (RMS) roughness height and the roughness parameter ( $R_a$ ).<sup>35</sup> The RMS value is the most common surface roughness

representation by estimating an arithmetic average of the peak heights and valleys from the mean surface. The  $R_a$  value is a similar representation which measures and averages five of the highest peaks to the five lowest valleys across a sampling length.

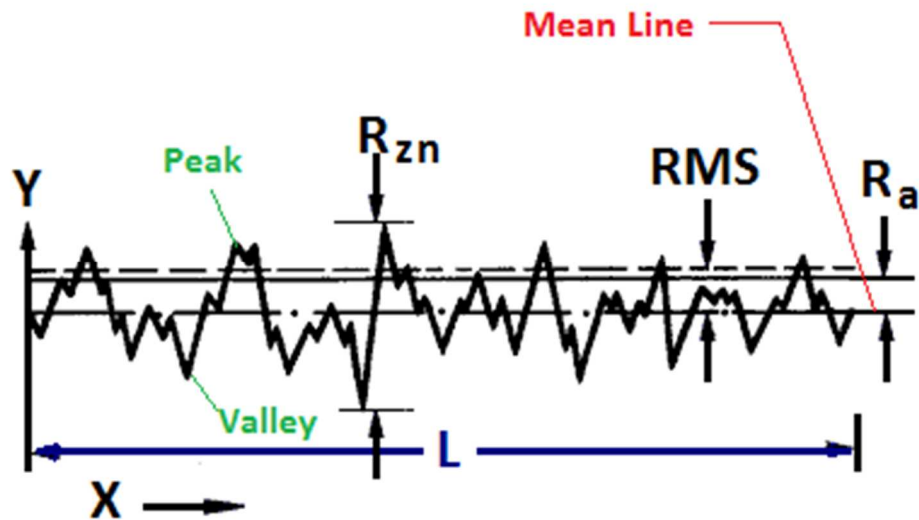


Figure 21. Material Surface Roughness<sup>35</sup>

The surface roughness of the skin can be obtained from the data sheet of the selected bladder material. The estimation of the minimum volume can be generalized as a function of the area of total material needed for the inflatable and the surface roughness.

A circular pillow-shaped drag brake inflatable with an inflated cross sectional area of  $1 \text{ m}^2$  contains a total of  $3.4 \text{ m}^2$  of Mylar material. The surface roughness of the Mylar sheets employed in this investigation, as provided by the manufacturer's data sheet, is  $R_a = 38 \text{ nm}$ . For this case, the minimum volume computed from the surface roughness is  $1.3 \text{ cm}^3$ . Accordingly,

the resulting volumetric expansion of the minimum volume occupied by residual air, due to change in ambient pressure, is characterized in Figure 22. Even though the likely differences in residual pressures (from ambient) during manufacture are relatively small, the slightest differences in differential pressure, between the ambient pressure and internal pressure of the inflatable, will enhance auto-inflation. Because it is not possible to eliminate this residual volume, the evacuation of the inflatable during fabrication was feasible to lower the residual air pressure at the minimum volume, thus lowering the volumetric expansion and auto-inflation potential.

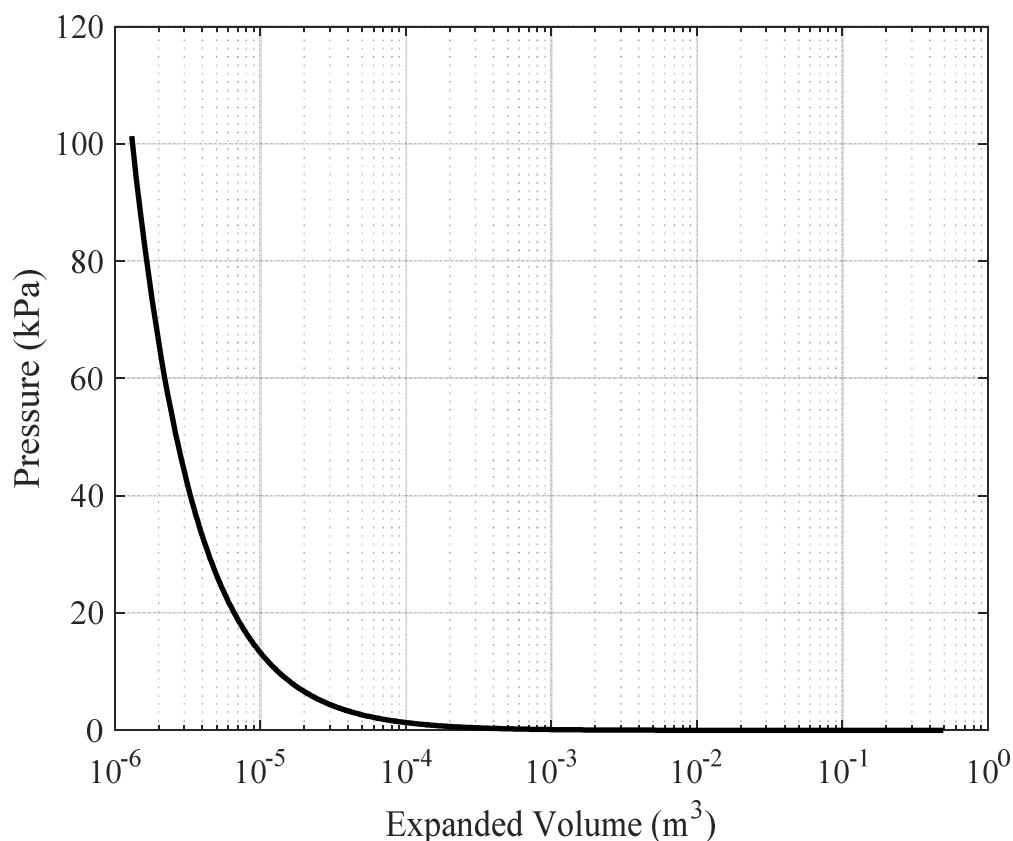


Figure 22. Volumetric Expansion of Minimum Inflatable Volume (1.3064 m<sup>3</sup>) vs. Change in Ambient Pressure

## CHAPTER IV

### THERMAL MODEL

Once the CubeSat drag device is deployed, solar heating will be utilized to heat the deflated unit, providing the required energy for sublimation. Consequently, the in-orbit thermal environment needs to be reliably modeled in order to predict the inflation potential for the drag brake. The thermal model developed in this chapter can demonstrate the utility of this drag brake design.

The *Echo I* satellite was launched into an orbit that exposed the satellite to continuous sunlight for the first two weeks of its orbit.<sup>36</sup> Under those conditions, the sublimating compounds could be heated continuously, achieving maximum performance. A continuous sunlight orbit was required for the *Echo I* satellite to allow the slower sublimating anthoquinone compound to maintain a consistent vapor pressure thereby maintaining the shape of the pressurized satellite for the two week test period.

The formulation of a detailed thermal model for an inflating drag brake geometry can be rather challenging. For that reason, in order to simplify the calculations, the thermal model employed in this study has assumed that the drag brake is spherical. Additionally, due to the very low vacuum conditions in space, aerodynamic heating is negligible, eliminating any convective heat transfer potential. Radiative heat exchange is the only external energy source considered in the model.

## External Incident Radiation Sources

The interaction of a spacecraft and its thermal environment was characterized employing three external incident radiation sources: (1) direct solar radiation from the sun,  $q_{direct}$ , (2) Earth-reflected/albedo radiation,  $q_{albedo}$ , and (3) Earth-emitted radiation,  $q_{earth}$  (Figure 23).

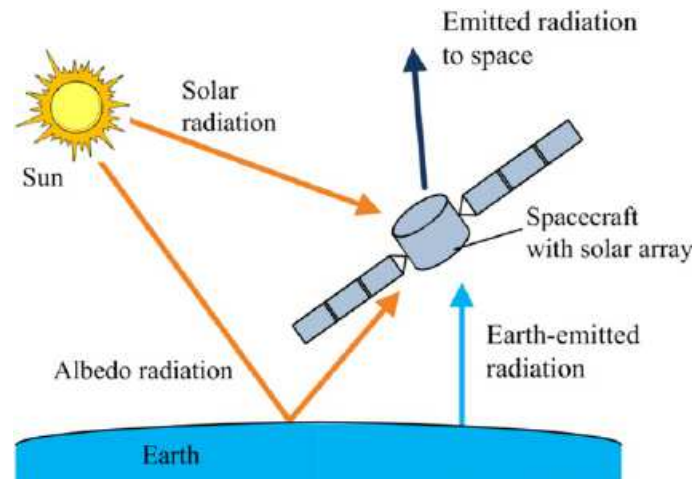


Figure 23. Typical Spacecraft Thermal Environment

The direct radiation from the Sun that is absorbed by the spacecraft is dependent on the solar radiation intensity constant,  $J_s$ . At the average distance from the Sun, outside of Earth's atmosphere, the solar radiation intensity constant is  $\sim 1371 \text{ W/m}^2$ .<sup>37</sup> If  $\alpha_s$  is the solar absorptance of the surface, and  $A_{direct}$  is the projected area receiving direct solar radiation, the total direct radiation received by the spacecraft.

$$q_{direct} = J_s \alpha_s A_{direct} \quad (17)$$

Albedo radiation is the reflected solar radiation received from the surface of Earth. This expression is dependent on the average albedo value,  $a$ . The albedo factor for Earth can vary drastically from 0.8 (from clouds) to 0.05 (over surfaces like water and forest). Since changes occur rapidly in relation to the thermal inertia of most spacecraft, the average albedo values for Earth are between 0.31 and 0.39.<sup>37</sup> Assuming an average albedo of 0.31, the total albedo radiation received by the spacecraft can be estimated as the following, where  $F$  is the view factor and  $A_{albedo}$  is the projected area receiving albedo radiation.

$$q_{albedo} = J_s a F \alpha_s A_{albedo} \quad (18)$$

The view factor for estimating the solar radiation reflected from the Earth is strongly-dependent on the actual orbit of the spacecraft. Even though the particular view factor still relies on the differential area definitions defined in Figure 25,<sup>39</sup> the Earth's surface can completely fill the field of view, and it is possible for the view factor to exceed unity, as shown in Figure 26.

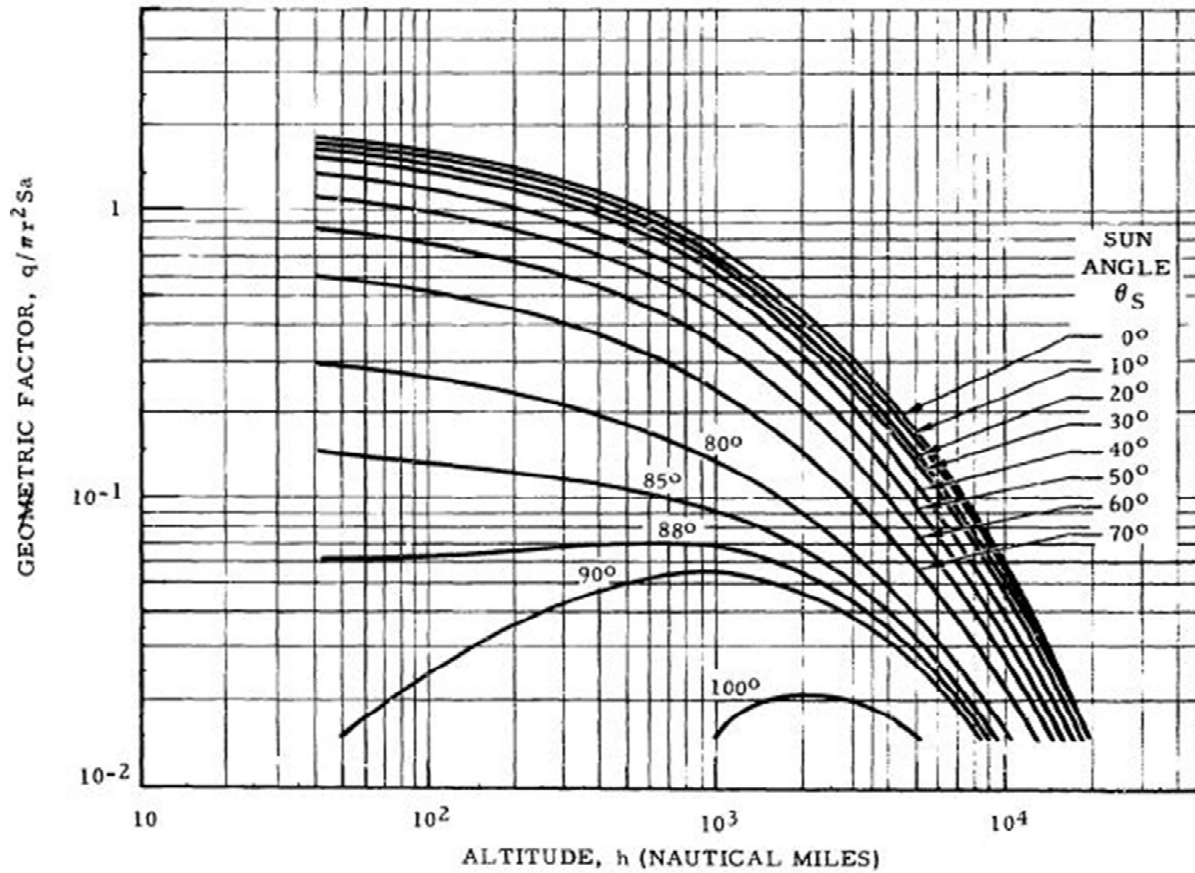


Figure 24. Approximate View Factors for Earth Reflected Solar Radiation Incident to a Sphere

Infrared radiation from the Earth's surface must also be considered. Its approximate surface intensity of  $237 \text{ W/m}^2$ , has been assumed.<sup>37</sup> However, the intensity on orbit is proportional to the inverse-square of the altitude. Consequently, the characteristic planetary radiation intensity,  $J_p$ , can be estimated utilizing the radius of the orbit,  $R_{orbit}$ , as

$$J_p = 237 \left( \frac{R_E}{R_{orbit}} \right)^2 \quad (19)$$

and the planetary radiation incident on the spacecraft surfaces depends on  $J_p$ , the infrared surface emissivity,  $\varepsilon$ , and the projected area that “sees”,  $A_{planetary}$ . i.e.

$$q_{earth} = J_p \varepsilon A_{planetary} \quad (20)$$

## Orbital Mechanics

The equilibrium spacecraft surface temperatures depend on its position with respect to the Earth and Sun. Due to the amount of time that a spacecraft spends in Earth’s shadow and in sunlight, an accurate representation of spacecraft position is crucial in characterizing its dynamic thermal response. Six orbital parameters are used to characterize an orbit and the location of a spacecraft, as shown in Figure 26: (1) semi-major axis,  $a$  (size of the orbit) (2) eccentricity,  $e$  (shape of the orbit), (3) inclination,  $i$  (orientation of the orbit with respect to the Earth’s equator) (4) argument of perigee,  $\omega$  (location of perigee with respect to Earth’s surface) (5) ascending node,  $\Omega$  (location of the ascending and descending orbit locations with respect to the Earth’s equatorial plane) (6) true anomaly,  $\nu$  (instantaneous location of the satellite with respect to the perigee). The derivation of the satellite position vector with respect to the six orbital parameters is described in Appendix A.

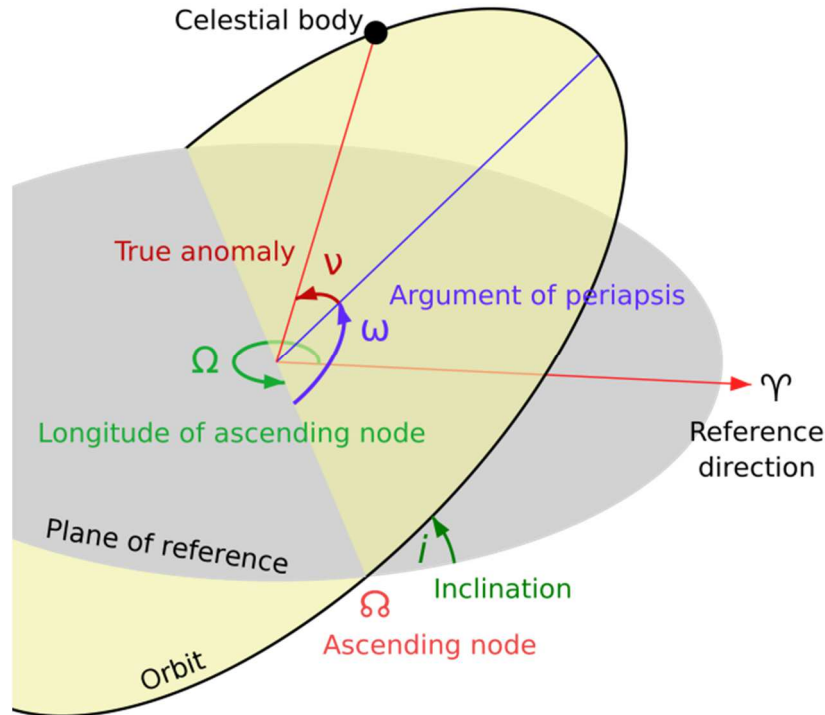


Figure 25. Geometry of Orbital Elements

The eclipse interval of an orbit is defined as the location in the orbit that a spacecraft is in the shadow of Earth. During this time, the direct solar and albedo radiation inputs will be terminated from the satellite. Because two major external radiation sources are “cut-off” in the eclipse, the time a spacecraft is present in the eclipse will directly affect the severity of the temperature fluctuations of the satellite.

Assuming that the Sun creates a cylindrical umbra with parallel sun rays, Figure 27 illustrates the spacecraft position vector,  $R_{sc}$ , just before entering/leaving the umbra, the Earth-Sun vector,  $R_S$ , and the Earth radius,  $R_E$ . The line of sight vector from the spacecraft to the sun, creates two right triangles with the spacecraft position vector, and the Earth-Sun vector, with angles  $\theta_1$  and  $\theta_2$ . Both,  $\theta_1$  and  $\theta_2$ , can be determined as follows.

$$\theta_1 = \cos^{-1} \frac{R_E}{|R_{sc}|} \quad (21)$$

$$\theta_2 = \cos^{-1} \frac{R_E}{|R_s|} \quad (22)$$

Consequently, the time and position in an orbit where the spacecraft will enter or leave the umbra is dependent on  $\theta_1$ ,  $\theta_2$ , and the angle between the Earth-Sun line and the spacecraft position vector,  $\theta_s$ . Under these circumstances, a spacecraft will experience Earth's shadow when  $\theta_s \geq \theta_1 + \theta_2$ , and a solar line-of-sight vector does not exist. When  $\theta_s < \theta_1 + \theta_2$ , the spacecraft is in sunlight, with an associated line-of-sight. Thus, the position and time in orbit where the spacecraft enters or leaves umbra can be defined utilizing  $\theta_s = \theta_1 + \theta_2$ .

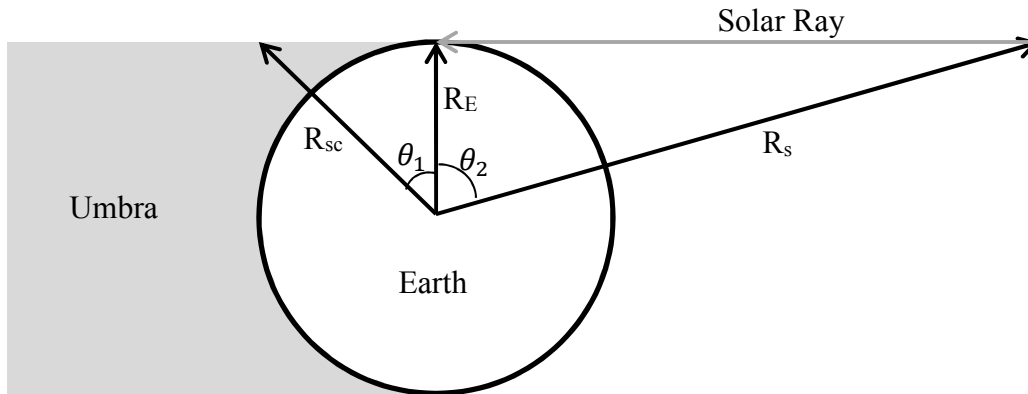


Figure 26. Earth Cylindrical Umbra from Parallel Solar Rays

## Thermal Environment

Surface equilibrium temperatures are determined by the thermal balance between the heat received and emitted by the spacecraft. Therefore, all measurable heat sources in the spacecraft

thermal environment must be characterized in order to estimate an accurate dynamic thermal response of a spacecraft.

The three external incident radiation sources have just been defined. Additionally, internally-dissipated heat,  $Q_{internal}$ , resulting from internal heat generation is another source. Furthermore the surfaces radiate heat to deep space. Since spacecraft surfaces are not blackbodies, they also emit radiation, which has been approximated utilizing grey body emissivity  $\varepsilon$ . The energy radiated from a spacecraft surface at absolute temperature,  $T$ , back into space can be expressed as:

$$q_{space} = \sigma T^4 \varepsilon A_{surface} \quad (23)$$

Recognizing that the spacecraft surfaces are subjected to rapid changes in overall heating, the heat balance representing the rate of change of the surface temperature of a spacecraft in terms of the mass of the spacecraft surface,  $m$ , its specific heat,  $C$ , its instantaneous temperature,  $T$ , and time,  $t$ , is

$$mC \frac{dT}{dt} = J_s \alpha A_{solar} + J_s a F \alpha A_{albedo} + J_p \varepsilon A_{planetary} + Q_{internal} - \sigma T^4 \varepsilon A_{surface} \quad (24)$$

By using the heat balance equation, the non-steady temperatures of the drag brake as a function of time and position in orbit can be estimated to characterize the inflation potential.

A spherical drag brake structure constructed from a Mylar membrane was used in this analysis, with properties given in Table 2. The surface temperatures and thermal dynamics of a spacecraft, defined in the heat balance equation, are dependent on the thermal mass of the material surface. For a material mass of 69.6 g and a specific heat of 1172 J/kgK, the modeled

drag brake had a thermal mass of 81.6 J/K. In terms of its ability to absorb and store heat, thus reducing temperature oscillations, the thermal mass of the of drag brake is relatively low in comparison to the cross sectional area. Therefore, the drag brake structure was expected to have rapid thermal response with the thermal environment.

Table 2. Drag Brake Material Properties

Material	Mylar
Absorbance, $\alpha$	0.1
Emittance, $\epsilon$	0.03
Specific Heat	1172 J/kgK
Cross Sectional Area	1.00 m <sup>2</sup>
Thickness	0.0127 mm
Density	1390 kg/m <sup>3</sup>
Mass	69.6 g

The heat balance equation was simulated in MATLAB using a finite difference method to determine the transient thermal response over a complete orbit. For a circular orbit altitude of 1000 km, with an inclination of 0°, the external incident radiation flux on the drag brake is depicted in Figure 28 with respect to the true anomaly. Direct infrared Earth radiation is continuous. For a spacecraft with a low thermal mass, the substantial deficit of incident heating flux when passing Earth's shadow can present extreme temperature fluctuations.

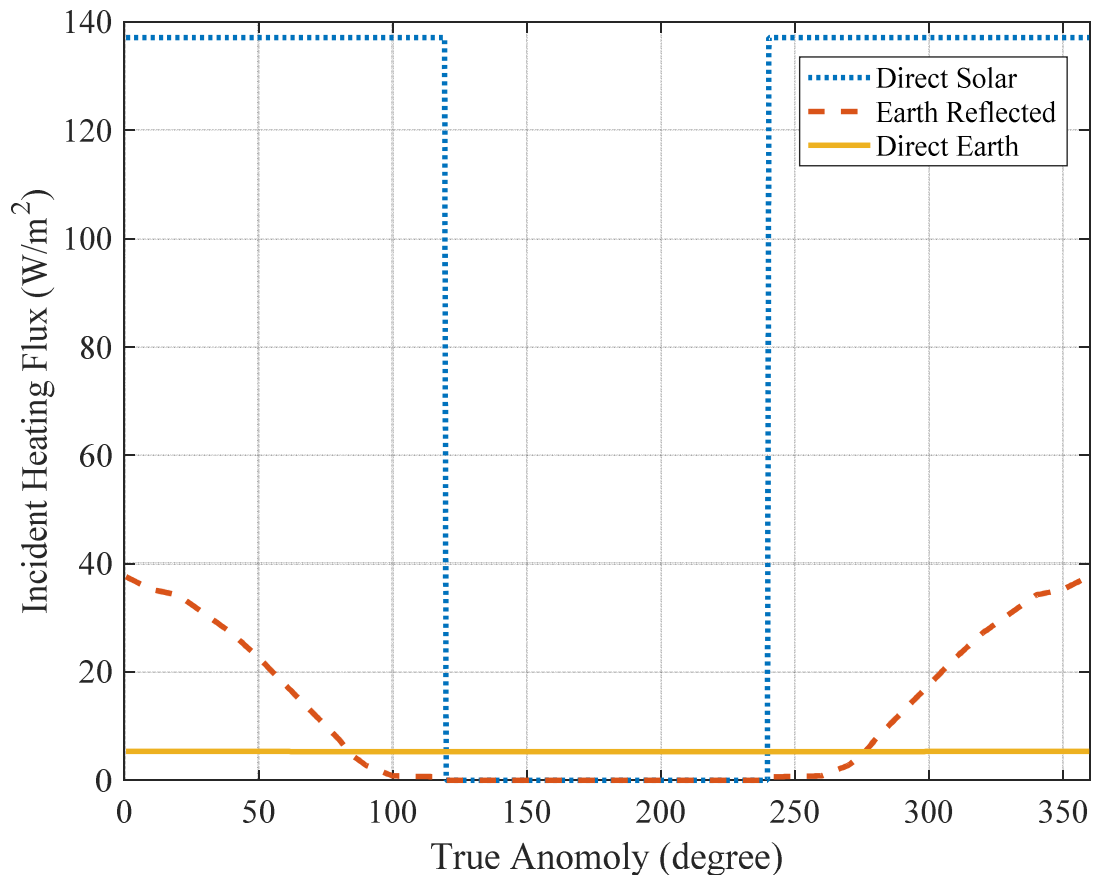


Figure 27. Incident Heat Flux for a Spherical Mylar Drag Brake ( $H=1000\text{km}$ ,  $i=0$ )

Subsequently, the thermal response of the drag brake for a 1000 km circular orbit for inclinations of  $0^\circ$ ,  $45^\circ$ ,  $58^\circ$ , and  $60.2^\circ$ , were simulated, and are shown in Figure 29. Although the thermal mass of the benzoic acid powder was not considered in this analysis, the small quantity of powder needed is not expected to significantly influence the surface temperatures of the drag brake.

At an orbital inclination of  $0^\circ$ , the drag brake spends the most time in the shadow resulting in the largest temperature fluctuation in its orbit. As a result, the drag brake would

experience a temperature cycle from  $-103.2^{\circ}\text{C}$  to  $131.5^{\circ}\text{C}$ , or a difference of  $234.7^{\circ}\text{C}$ . For an orbital inclination of  $45^{\circ}$  and  $58^{\circ}$ , the drag brake surface temperature will experience a change of  $199.6^{\circ}\text{C}$  and  $224.4^{\circ}\text{C}$  in one orbit respectively.

As the inclination of the orbit increases, the temperature variation amplitude decreases. However, when the drag brake passes through the slightest part of the Earth's shadow there is a significant temperature drop. For orbits with inclinations greater than  $60.2^{\circ}$ , the drag brake can be in continuous sunlight. For continuous sunlight orbits, thermal excursions are significantly smaller, ranging between  $109^{\circ}\text{C}$  and  $119.8^{\circ}\text{C}$ .

Because the sublimating compound relies on solar heating for the required inflation pressures, the large documented temperature fluctuations can be rather limiting. Despite the orbital inclination, the maximum surface temperature the drag brake can encounter ranges between  $119.8^{\circ}\text{C}$  to  $131.5^{\circ}\text{C}$ . These temperatures represent estimated equilibrium vapor pressures between the range of 4.6 torr and 9.1 torr; sufficient for the initial inflation of the drag brake.

However, it was determined that the drag brake will encounter large temperature fluctuations when passing through Earth's shadow. At an orbital inclination of  $0^{\circ}$  the inflatable will encounter a minimum surface temperature of  $-103.2^{\circ}\text{C}$  and a maximum surface temperature of  $131.5^{\circ}\text{C}$ . Therefore, the temperature-dependent sublimating benzoic acid powder would experience equilibrium vapor pressure fluctuations between  $9 \cdot 10^{-16}$  torr and 9.1 torr. The concurrent vapor pressure fluctuation is highly undesirable when relying on the internal pressure to maintain the inflated drag brake during a complete orbit. For this reason, a rapid rigidization technique is needed in order to maintain the inflated geometry and structural rigidity. Although

the analysis was performed for a circular orbit at an altitude of 1000 km, further analysis can be performed at other orbital parameters.

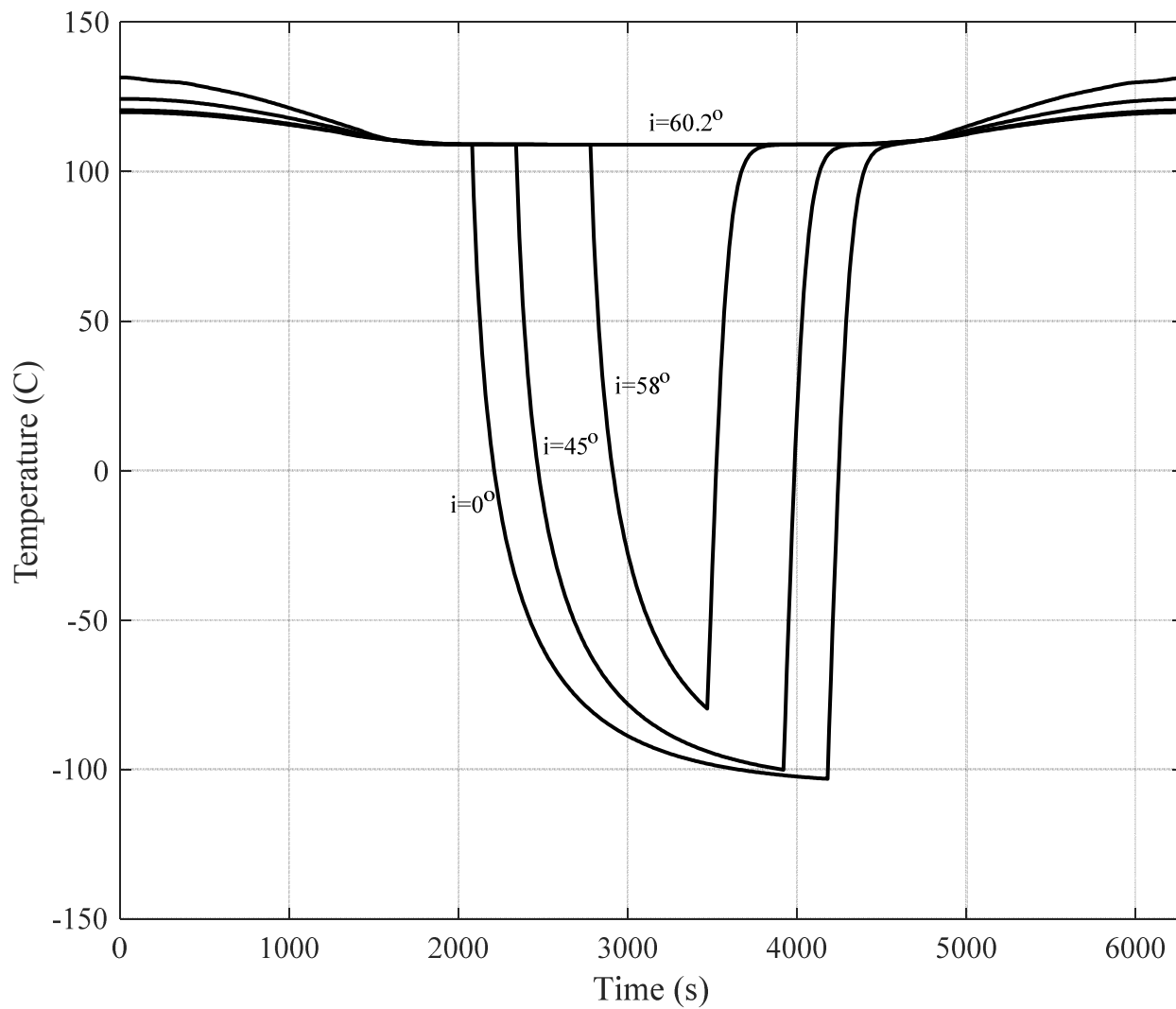


Figure 28. Thermal Response of Drag Brake at 1000 km Altitude for Various Orbital Inclinations

## CHAPTER V

### EXPERIMENTAL INVESTIGATIONS

A differential pressure test and a thermal vacuum test were conducted to investigate the functionality of a sublimating compound inflation system for a CubeSat drag device. Since inflation of the test article results from the pressure difference between the vacuum chamber pressure and the internal sealed membrane pressure, it was necessary to anticipate the pressure difference needed for inflation. However, it is extremely difficult to measure the small pressure differences needed to effect transient inflation behavior and the pressure differences induced during the inflation process. Consequently, tests were conducted to relate imposed internal pressure differences to the actual inflated volume. These data could be used to correlate the inflation pressure differences, while avoiding the need for any sort of membrane stress sensors for inferring pressure differences. A thermal vacuum chamber test has been performed to validate the sublimating compound inflation system in a simulated space environment. The development of an experimental test article and subsequent development and execution of a test plan is discussed in this chapter.

#### **Test Article Fabrication**

The actual fabrication process became important because it was necessary to examine the evacuation procedure for the planned tests, in order to limit auto-inflation resulting from residual air. The circular pillow-shaped geometry could be fabricated easily by bonding two circular Mylar disk sheets along their circumferences, reducing manufacturing complexity and the number of joints that would result from more complicated gore geometries. For these tests, a

reduced-scale inflatable was employed to observe the vacuum chamber inflation characteristics. It was decided that the test inflatable would be scaled down to a deflated radius of 21 cm.

An overlap was added to the drag brake boundary to provide a 1 cm bead space to properly seal the test article. The bonding method had to provide a hermetic seal that could withstand the anticipated pressure differences to be encountered in the vacuum facility. Surface characteristics of Mylar made selecting a compatible bonding adhesive difficult. After examining alternatives, heat sealing was selected as the preferred bonding procedure.<sup>40</sup> The effectiveness of a heat seal is a function of heating duration, contact temperatures and the pressure applied during the joining process.<sup>40</sup>

It was determined that seemingly inconsequential quantities of residual air could lead to potentially-destructive, uncontrolled inflation. To reduce the probability of rupture, careful consideration was given to the amount of air that could be tolerated inside the inflatable test article. For the thermal vacuum chamber test, evacuation of the inflatable during manufacture was necessary to limit the amount of residual air. Although it is not possible to evacuate all the air internally, an effort was made to evacuate the inflatable to 1 torr, prior to delivering the test articles for testing in the NASA LaRC vacuum chamber. To prevent possible damage to the pre-treatment vacuum pump that could result from benzoic acid vapor precipitation in the pumping unit, a corrosive gas roughing pump, capable of evacuating to pressures as low as  $10^{-3}$  torr was employed.

The test article air removal vacuum setup is shown in Figure 30. The roughing pump was mated with the test article utilizing vacuum tee fitting. One leg of the tee was attached to an absolute pressure sensor, and a vacuum seal-off valve was the other element of the tee. Once the

desired vacuum pressure was achieved, the vacuum valve between the test article and roughing pump was closed and the deflated test article enclosing the specific mass of benzoic acid powder was heat sealed to create an effective hermetic seal.

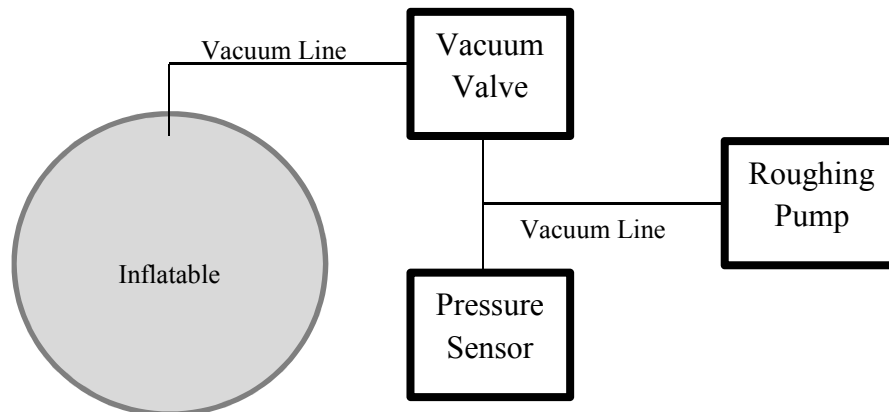


Figure 29. Air Removal Vacuum Setup

### Test Article Geometric Estimations

It is very difficult to measure accurately the difference between internal inflatable pressure and the external pressure being maintained in a vacuum chamber. Insertion of an absolute pressure sensor connection in the stem of the uninflated bladder would introduce too much residual air for vacuum tests. Employing a strain gage, mounted on the skin of the membrane was rejected because it would distort the inflated shape of the bladder. As an alternate approach, this thesis has investigated the feasibility of utilizing the calculated volume of the partially-inflated bladder as a correlated measure of differences between the internal pressure and the external ambient pressure.

At any internal pressure, the inflatable can be modeled as an ellipsoid shape. If the three-dimensional shape representation can be fitted to an approximated ellipsoid, then the computed volume of the nominal ellipsoid should agree to within some tolerance of the actual volume of the inflatable.

*Microsoft Kinect for Windows* was employed to map the shape of the test article surface under varying test conditions. Acquired images could be processed to generate a surface point cloud that could be used for measurements of the test article, utilizing *3-D reconstruction*.<sup>2</sup> The *Kinect* has been one of the most popular consumer-grade depth sensors while also providing an RGB camera and multi-array microphone for full-body 3-D motion capture, facial and voice recognition.<sup>41</sup> Specifications for the device are summarized in Table 3.<sup>42</sup>

Table 3. *Microsoft Kinect* Specifications

Parameter	Value	
<b>Spatial Resolution</b>	RGB/Depth/IR	640 pix x 480 pix
	X	1.70mm/pix/meter
	Y	1.64mm/pix/meter
<b>Depth Range</b>	Default	0.8m-4.0m
	Near	0.4.-3.0m
<b>Depth Resolution</b>	2mm to 40 mm (depending on depth)	
<b>Frame Rate</b>	30 fps	
<b>Field of View (FOV)</b>	43° Vertical by 57° Horizontal	
<b>Tilt Range</b>	27° Vertical	
<b>Focal length</b>	Depth	5.453 0.012mm
	RGB	4.884 0.006mm
<b>IR Wavelength</b>	830nm	
<b>Baseline Length</b>	75 mm	

The *Kinect* utilizes a class 1M infrared laser (IR emitter) and an Aptina MT9M001 complementary metal-oxide-semiconductor (CMOS) sensor (IR camera).<sup>41</sup> Both of these devices operate in stereo as an active triangulation system for acquiring depth data. The infrared laser is projected through a diffraction grating which produces a speckle pattern of IR dots onto the image scene. The reflected pattern is captured by the IR camera and is correlated with a reference speckle pattern corresponding to a plane at a known distance. Depending on whether the object is further or closer to the imager than the reference, the speckle pattern is shifted to adjust the perspective center of the IR camera, along the baseline of the IR laser and IR camera. A stereo triangulation algorithm is used to obtain an estimate of the shift, or the disparity, between the patterns, producing a disparity-depth relationship. Figure 31 shows a schematic representing the disparity-depth model that is utilized by the *Kinect*. In the schematic,  $Z_k$  is the distance to the object plane,  $Z_o$  is the distance to the reference plane,  $f$  is the focal length of the imager,  $b$  is the baseline distance between the IR camera and IR laser projector and  $d$  is the disparity distance.<sup>43</sup>

Unfortunately, due to the reflectivity of aluminized Mylar, the IR camera could not capture the basic shape of the test article. It was found that less-reflective, 2.5 cm diameter, paper fiducial dots could be applied to the test article skin to capture and register the speckles on the IR camera. On that basis, the 3D representation of the inflatable surface for various internal pressures was used to obtain a fitted nominal ellipsoid that can agree within tolerance to the actual inflatable volume.

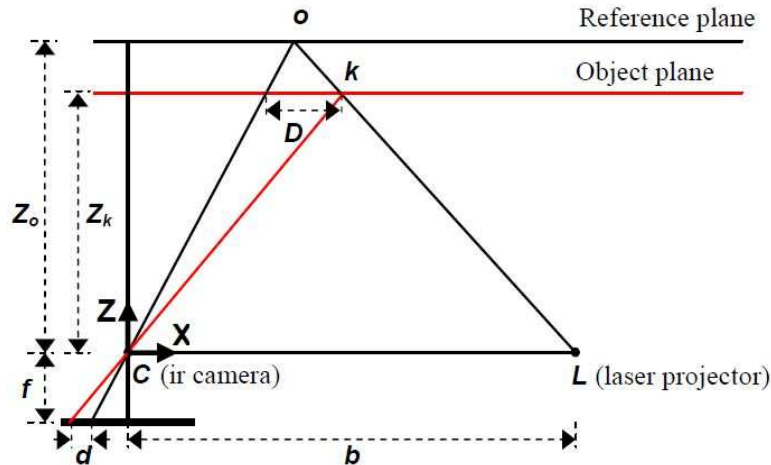


Figure 30. Depth-Disparity Model

### Differential Pressure Inflation Test

The inflated volume was determined by the difference between its internal pressure and its external pressure; therefore, inflated shape of the drag brake test article can be a direct measure of the differential pressure. A differential pressure test, or a static pressure test, can be performed at standard temperature and pressure to relate directly the inflation characteristics that will be observed in orbit. However, because the differential pressure is relative to the ambient pressure, and the anticipated pressure differences are very small relative to a standard atmosphere, precise determination of the actual differential pressures was a major challenge.

The differential pressure test setup is shown schematically in Figure 32. Careful consideration was given to the orientation of the test article during the ambient tests. If the inflatable was placed on a surface, deformation due to gravity would occur in comparison with its undistorted inflated shape. The test article was suspended beneath a tripod in the actual setup to prevent gravity-driven “footprint” effects. Since the differential pressures were so small,

buoyant density effects were minimized Differential pressures were produced utilizing air from a small air compressor, thus varying the internal pressure. Simultaneously, a differential pressure transducer was attached to the inflatable that could log the instantaneous internal pressure utilizing a *LabVIEW* program. Concurrently, 3-D point clouds of the inflatable surface were acquired and fitted to a nominal ellipsoid utilizing a least squares method in *Matlab* script. Data from the pressure transducer and the fitted ellipsoid approximation were used subsequently to correlate the internal pressure with respect to inflated volume. Multiple internal pressure data points were obtained from this test to create a database of results for estimating the geometric characteristics of the inflatable with respect to applied internal pressure. The results from these tests will be discussed in the next chapter.

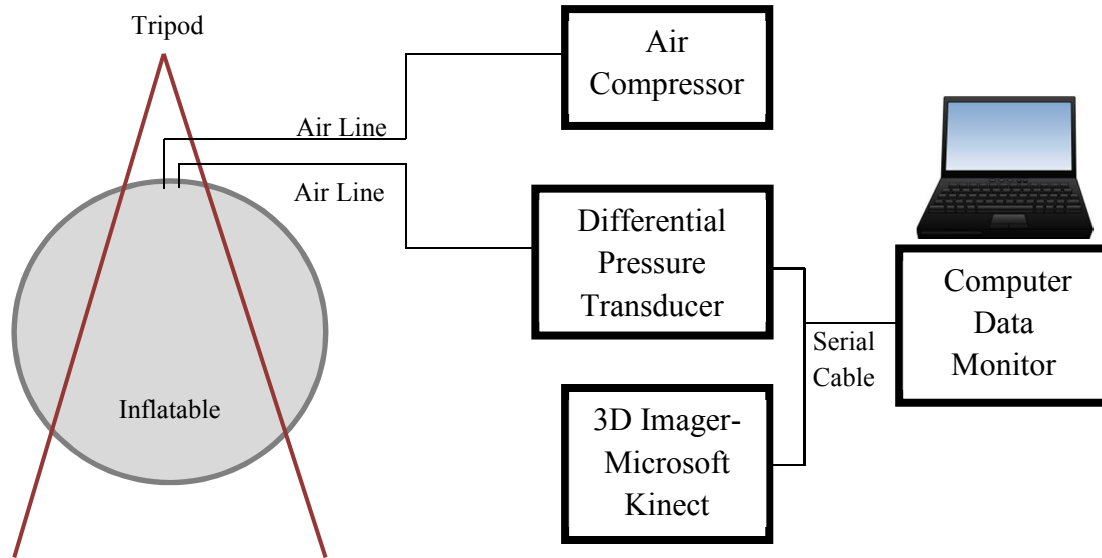


Figure 31. Differential Pressure Test Setup

## Thermal Vacuum Chamber Test

The primary objective of the thermal vacuum test was to evaluate the dynamics associated with drag brake inflation utilizing benzoic acid sublimation in a simulated space environment. Results from the test could demonstrate the feasibility of using sublimating benzoic acid powder as a gas generator for inflation, avoiding the storage bottles and valves associated with ordinary inflation systems. Additionally, the expansion processes that can occur with extremely small masses of residual air were considered in order to better understand its effect on the dynamics of inflation.

Preliminary thermal vacuum tests were conducted in a *Cascade TEK High Vacuum Oven* (Figure 33), located in Building 1250 at NASA Langley Research Center (LaRC). Although this vacuum oven is typically used for bake-outs or drying processes for space/flight hardware, the oven provides pressures in the high-vacuum range (between  $10^{-4}$  to  $10^{-8}$  torr) at temperatures up to 200 °C, thus simulating orbital environmental conditions. The vacuum oven was operated in accordance with NASA LaRC facility procedures.

The thermal vacuum test utilized two different test articles. The first test article contained only the residual air left after roughing pump evacuation during manufacture. This inflatable was folded in quarters to determine whether the internal pressure differential was sufficient to completely unfold the inflatable. Without the sublimating compound, the dynamics of the expansion due to residual air could be indicative of the overall auto-inflation significance. During the evacuation of the vacuum chamber, the ambient pressure and 3-D depth images of the test article surface were documented in an effort to estimate the test article volume at various vacuum chamber pressures, up to the maximum inflated volume. This test did not utilize the vacuum chamber heat platen.



Figure 32. Cascade TEK High Vacuum Oven

The second test article contained the desired quantity of benzoic acid powder for fully-inflating the Mylar bladder. This test was intended to characterize the functionality and performance of the subliming benzoic acid inflation system. During the test, the inflatable rested on the temperature-controlled heating platen to allow for conductive heat transfer, enabling the benzoic acid powder to be heated employing anticipated orbital temperatures. Three thermocouples were employed to measure the instantaneous platen temperature and two local Mylar surface temperatures on the top surface during inflation. The test setup is shown schematically in Figure 34.

Based on the maximum anticipated orbital temperatures from Chapter 4, the test article was to experience a nominal transient temperature test profile that reached a maximum platen

temperature of 125 °C, as represented in Figure 35. Once the chamber was evacuated, the platen and surface temperatures and 3-D depth images of the test article surface were documented in an effort to estimate the instantaneous volume while the heat platen temperature was ramped-up to 125 °C

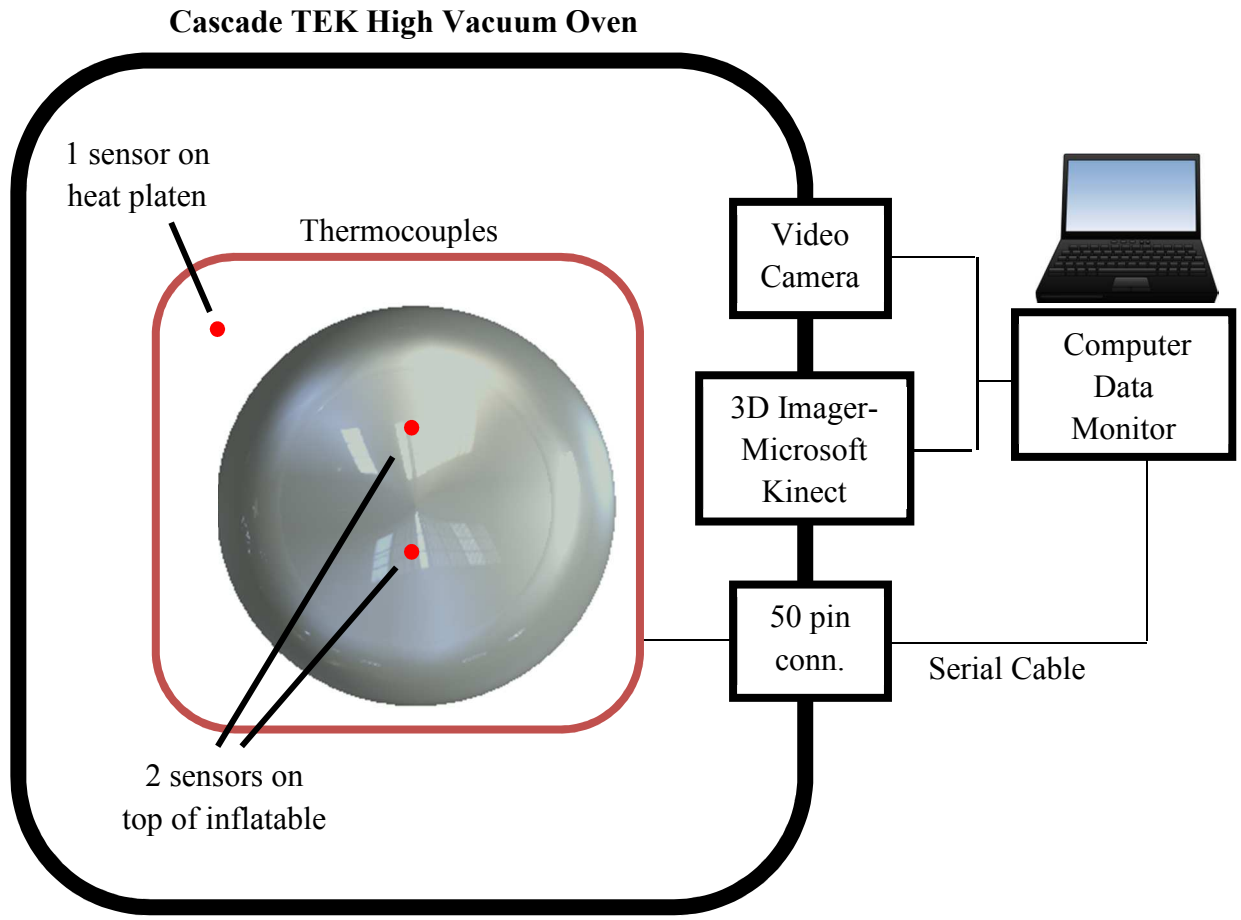


Figure 33. Thermal Vacuum Test Setup

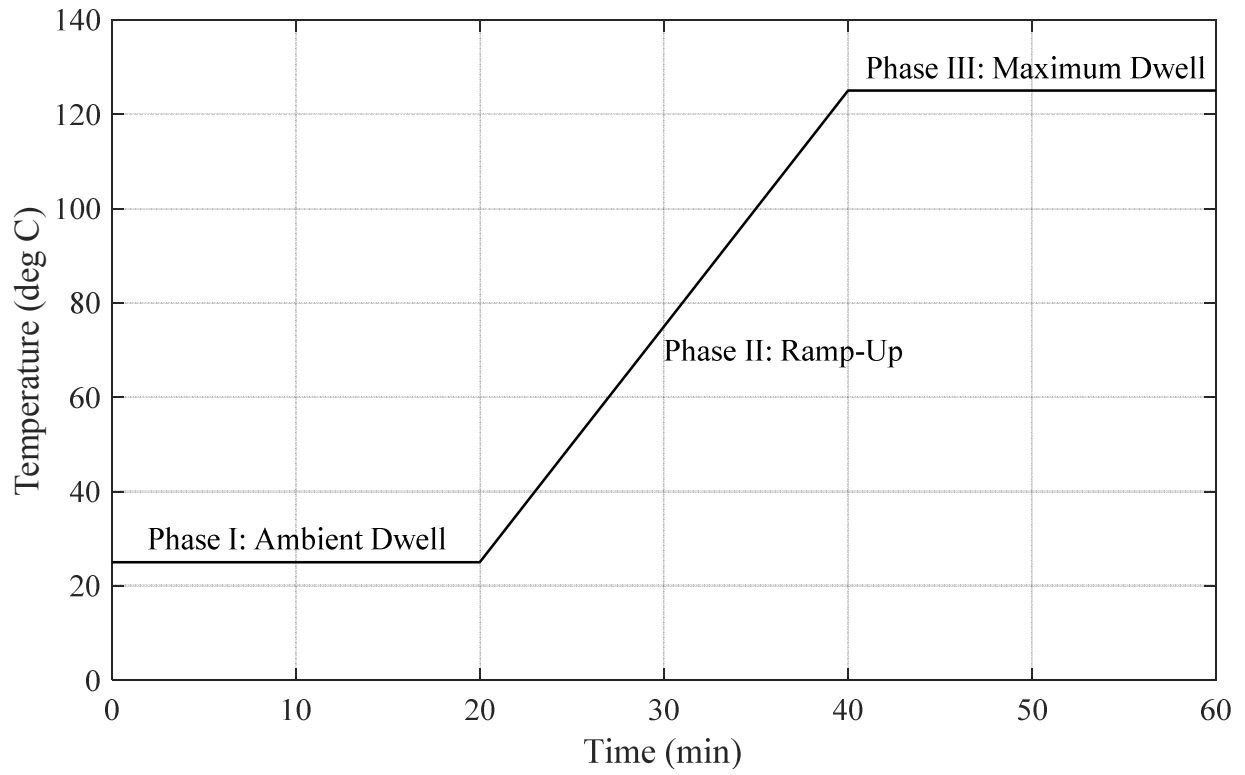


Figure 34. Thermal Vacuum Test Profile

## CHAPTER VI

### RESULTS

#### **Inflatable Internal Pressure – Volume Relationship**

The differential pressure tests were conducted at room temperature in an effort to relate the internal pressure difference to the volume of the inflatable, utilizing a 42 cm diameter Mylar balloon. The laboratory temperature was not varied in these feasibility tests, since it is expected that the volume and shape of the balloon, at any given pressure difference, is the controlling parameter.

In order to accurately approximate the three-dimensional surface of the bladder as an ellipsoid, a large number of surface data points was required. The initial 3-D point cloud, called the *raw 3-D point cloud*, was acquired employing the 3-D imager, as shown in Figure 36. When the fiducial dots were near the maximum observable radius of the partially-inflated test article, the projected area viewed by the 3-D measuring device became vanishingly small. Therefore, the circumferential plane was established manually and the raw surface location data points were mirrored with respect to the circumferential plane. In that way, a surface representation on the opposite-facing surface of the test article could be represented. This mirror image point cloud, or the modified point cloud, is shown in Figure 37.

The Yury Petrov Ellipsoid Fit MATLAB Script was used to represent the modified point cloud approximately as an ellipsoid.<sup>44</sup> The ellipsoid fit MATLAB script employs a linear least squares method to fit an ellipsoid to the polynomial:  $Ax^2 + By^2 + Cz^2 + 2Dxy + 2Exz + 2Fyz + 2Gx + 2Hy + 2Iz = 1$ . Figure 38 shows a fitted ellipsoid at a corresponding internal

pressure. The properties of the fitted ellipsoid were extracted from the program to determine the estimated semi-major radius, semi-minor radius, and volume of the test article.

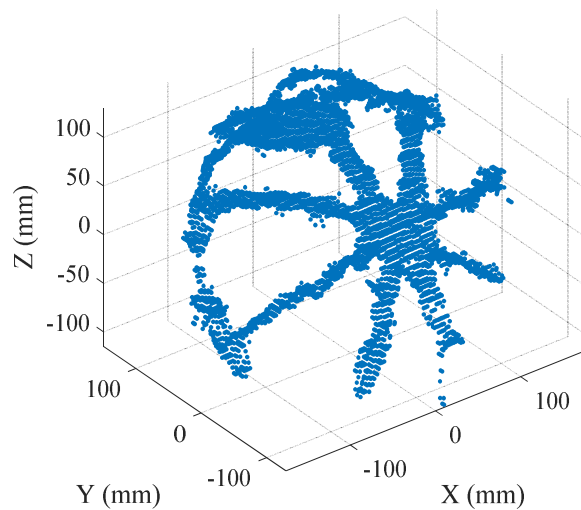


Figure 35. Raw Point Cloud: 3.2 torr

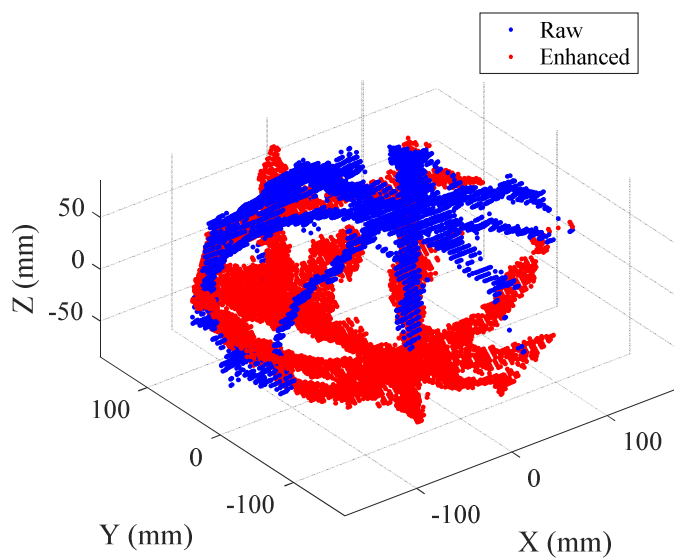


Figure 36. Enhanced Point Cloud: 3.2 torr

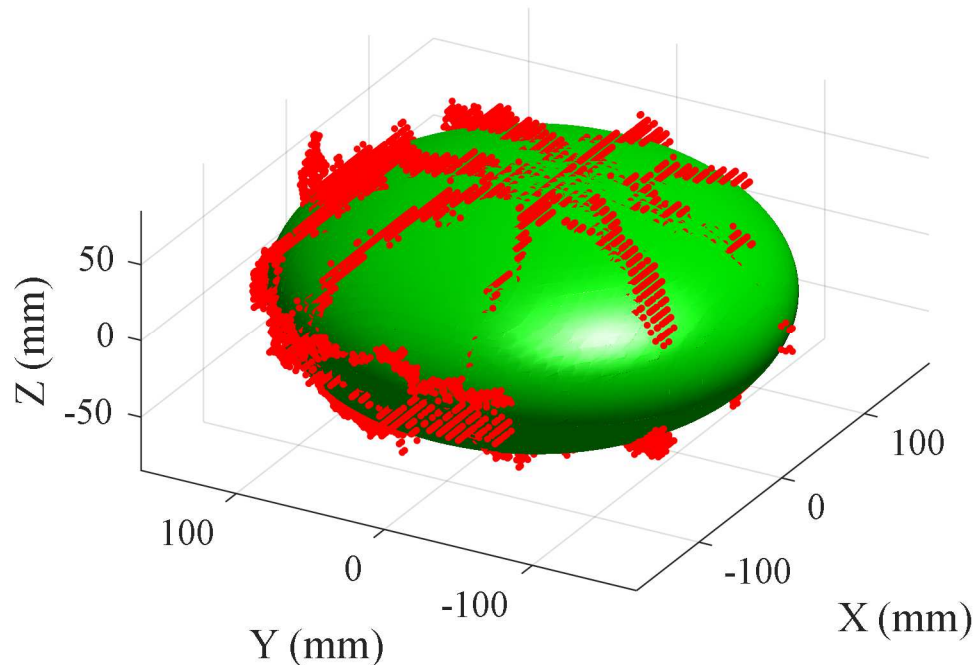


Figure 37. Modified Point Cloud Ellipsoid Fit: 3.2 torr

A total of 145 internal pressure data points were obtained for gage pressures between 0 and 15 torr. Each data point was fitted to obtain an approximate nominal ellipsoid estimate of the corresponding semi-major radius, semi-minor radius and volume of the inflatable. Figure 39 shows the resulting approximation for the semi-minor and semi-major radii with respect to the measured internal pressure difference. Since Mylar is relatively stiff, it can be seen that the semi-major radius decreases with increasing pressure, reaching its minimum limit of 158 mm at a pressure difference of approximately 5 torr. The semi-minor radius increases with increasing pressure difference, reaching a maximum limit of 101 mm, at an internal pressure of 10 torr.

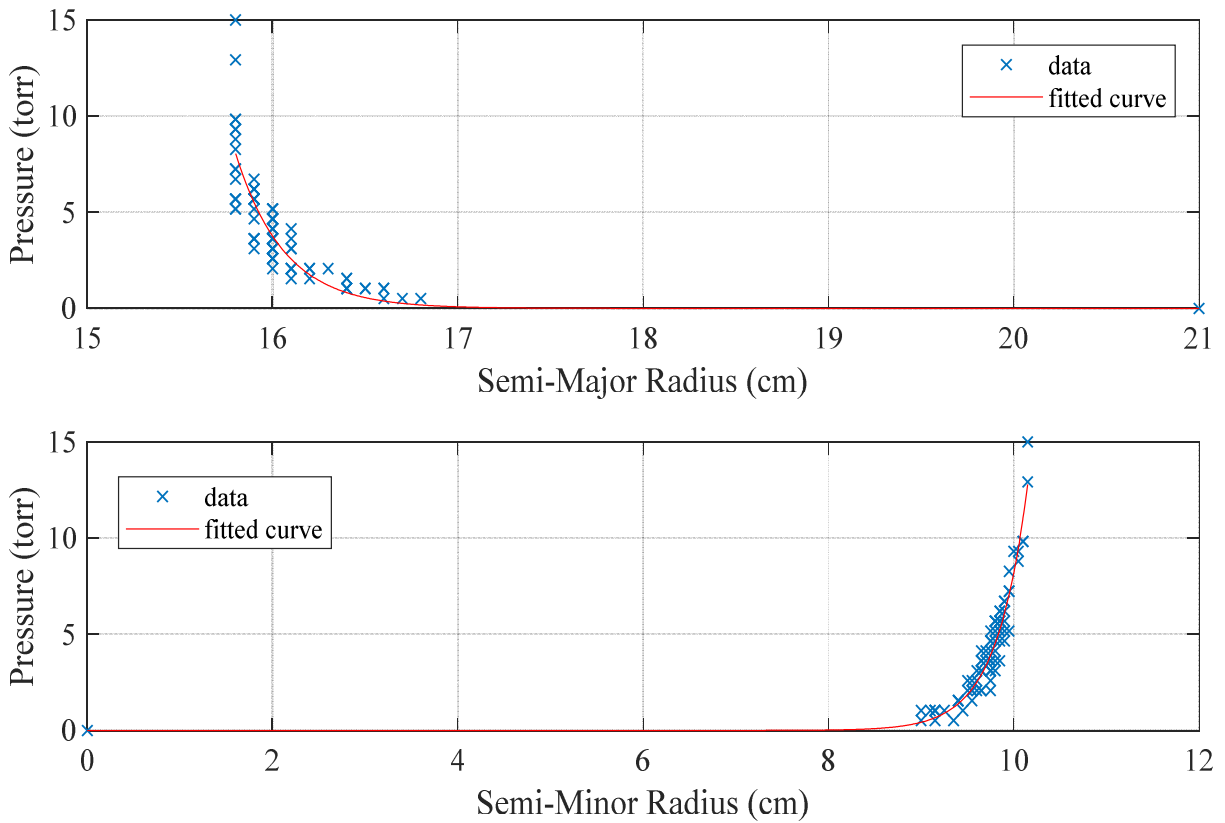


Figure 38. Semi-Major and Semi-Minor Radius vs. Internal Pressure Approximation

The estimated inflatable volume is shown as a function of internal pressure difference in Figure 40. The approximation represents the minimal differential pressure needed for full inflation. The data show that a fully-inflated volume of  $\sim 10300 \text{ cm}^3$  is achieved for a pressure difference of 0.5 torr.

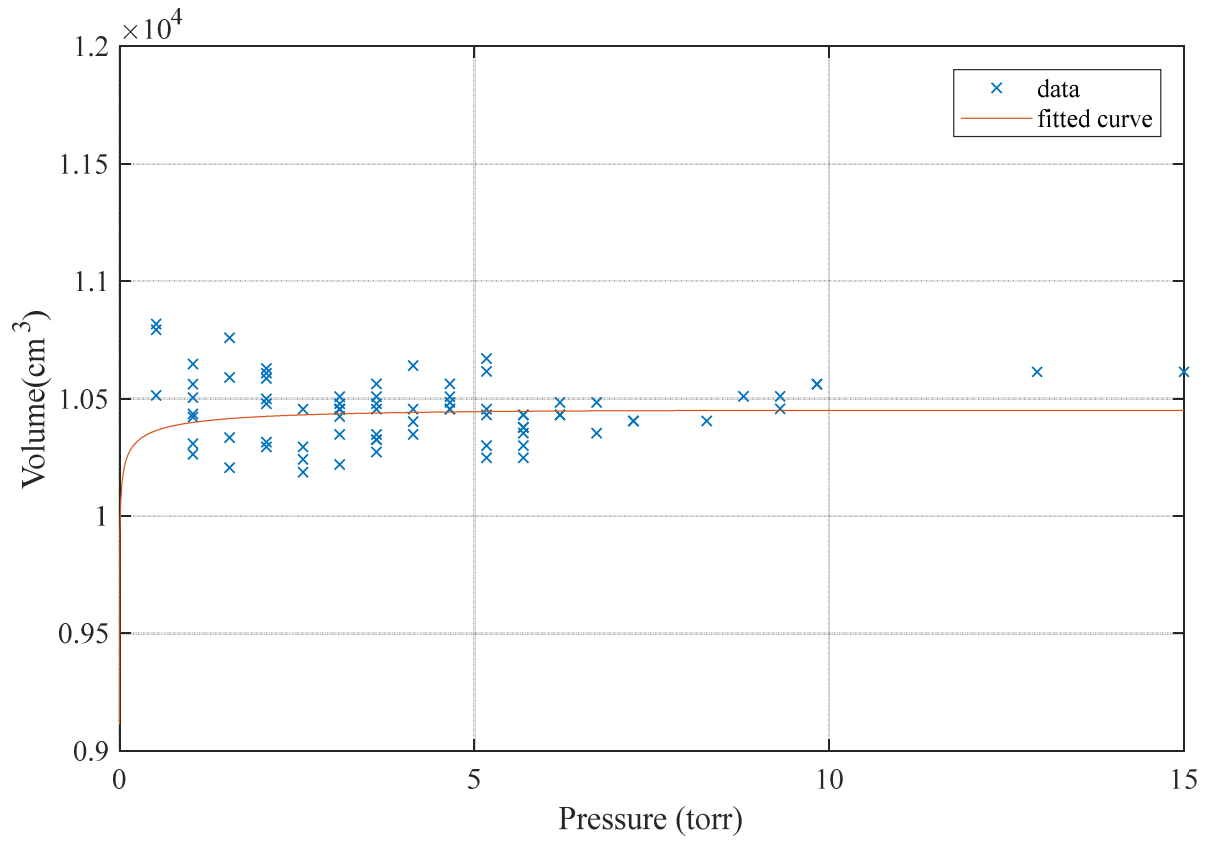


Table 4. Test Article Characteristics

Test Article	Contents	Deflated Radius	Evacuation Pressure
1	7.0g Benzoic Acid Powder & Air	21 cm	0.58 torr
2	Air	21 cm	0.50 torr

Figures 41 and 42 are images of the surface of the evacuated residual air test article and the benzoic acid charged inflatable, respectively. It was observed that the surface texture of the benzoic acid inflatable was rough in comparison with the “residual air” test article, due to the presence of the crystalline powder.



Figure 40. Air Inflatable Surface



Figure 41. Benzoic Acid Inflatable Surface

The air inflatable was folded in quarters to better understand the dynamics of expansion of residual air inside the inflatable. Figure 43 shows the folded inflatable at a chamber pressure of 12 torr. When the vacuum chamber reached 7.1 torr, the inflatable was observed to unfold from its initial quarter fold state (Figure 44). The residual air continued to expand at ambient chamber pressures of 5.1 torr (Figure 45), and at 2.9 torr, the inflatable unfolded completely, as shown in Figure 46. Expansion continues at 2.4 torr (Figure 47) until the ambient chamber pressure was equal to or less than an estimated internal pressure at 0.5 torr (Figure 48).

Once the test article reached its maximum limit, a three-dimensional depth image of the inflatable surface was taken to fit and obtain an estimate of the semi-major radius, semi-minor radius, and the associated volume of the air test article. At the maximum volume limit, the test article had an estimated semi-major radius of 165 mm, and semi-minor radius of 89 mm, with approximate volume of 10100 cm<sup>3</sup>. Results of the air inflatable test are summarized in Table 5.



Figure 42. Air Inflatable (12 torr)

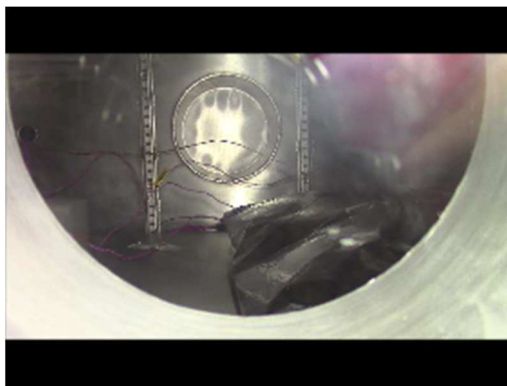


Figure 43. Air Inflatable (7.1 torr)

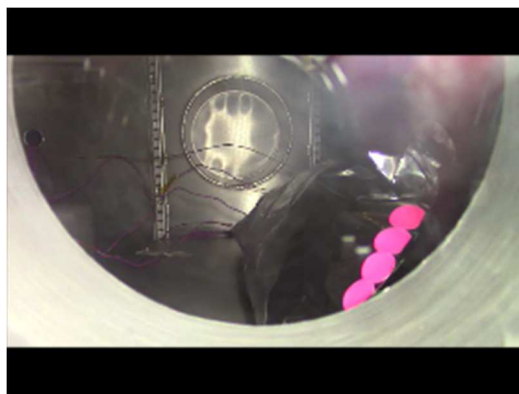


Figure 44. Air Inflatable (5.1 torr)

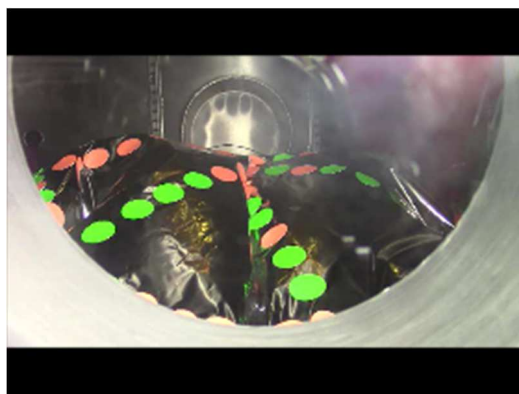


Figure 45. Air Inflatable (2.9 torr)

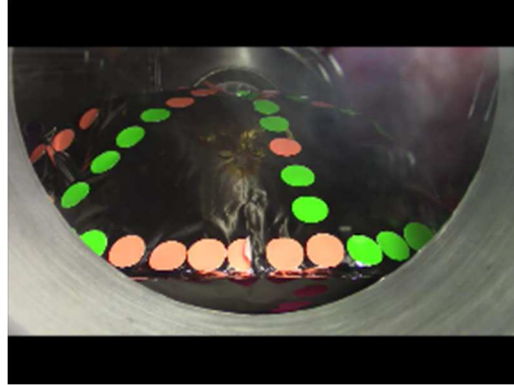


Figure 46. Air Inflatable (2.4 torr)



Figure 47. Air Inflatable (0.5 torr)

Table 5. Air Inflatable Results

<b>Contents</b>	Air
<b>Deflated Radius</b>	21 cm
<b>Evacuated Pressure</b>	0.5 torr
<b>Estimated Inflated Semi-Major Radius</b>	165 mm
<b>Estimated Inflated Semi-Minor Radius</b>	89 mm
<b>Estimated Inflated Volume</b>	10149 cm <sup>3</sup>
<b>Inflated Limit Ambient Pressure</b>	0.5 torr

The thermal vacuum test of the benzoic acid test article demonstrated the effectiveness of the sublimating benzoic acid inflation system for a CubeSat drag brake. The platen temperature profile was chosen to simulate the anticipated orbital temperatures in order to validate the inflation system functionality in a simulated environment. Once the chamber was evacuated, the temperature of the heat platen was ramped to 125 °C. Figures 49 through 54 show the inflatable at 20°C, 40°C, 60°C, 80°C, 100°C, and 126.8°C respectively during the temperature ramp. Additionally, thermocouples were placed on the top face of the inflatable to measure localized temperatures on the surface of the inflatable during the duration of the test. The associated upper surface temperature history is shown in Figure 55.

During the dwell period at ~125 C, the inflatable experienced a rupture along its seam, as shown in Figure 56. Concern over possible contamination of the vacuum chamber resulted in termination of the test before the top surface temperature reached steady-state. It was later determined that the internal pressure of the inflatable gradually peeled the seam resulting from a poor quality control of the heat seal.



Figure 48. Benzoic Acid Inflatable (20°C)



Figure 49. Benzoic Acid Inflatable (40°C)



Figure 50. Benzoic Acid Inflatable (60°C)



Figure 51. Benzoic Acid Inflatable (80°C)



Figure 52. Benzoic Acid Inflatable (100°C)



Figure 53. Benzoic Acid Inflatable (126.8°C)

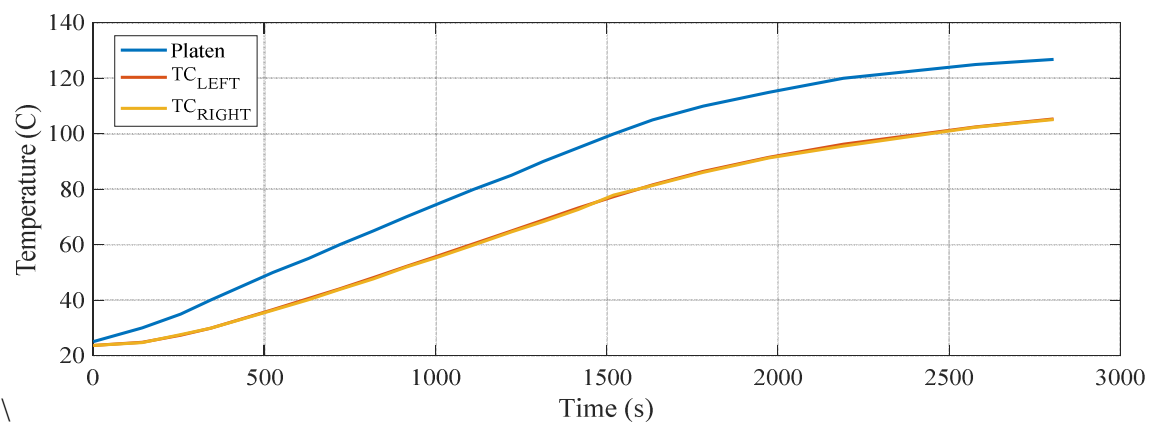


Figure 54. Temperature History of Benzoic Acid Test Article



Figure 55. Ruptured Benzoic Acid Test Article Showing White Benzoic Acid Residue

Between 20°C to 125°C, -D depth images of the inflatable surface were documented in 5°C intervals in an effort to characterize the semi-major, semi-minor radii, and associated volume at those temperatures. The estimated semi-major radius and the semi-minor radius values with respect to the heat platen temperature are shown in Figure 57. During the temperature ramp, there is a measureable decrease and increase in semi-major and semi-minor radii respectively. Figure 58 shows the relationship between the test article volume with respect to the platen surface temperature. From 20°C to 125°C, the approximate volume of the inflatable ranged from 10300cm<sup>3</sup> to 12000cm<sup>3</sup>.

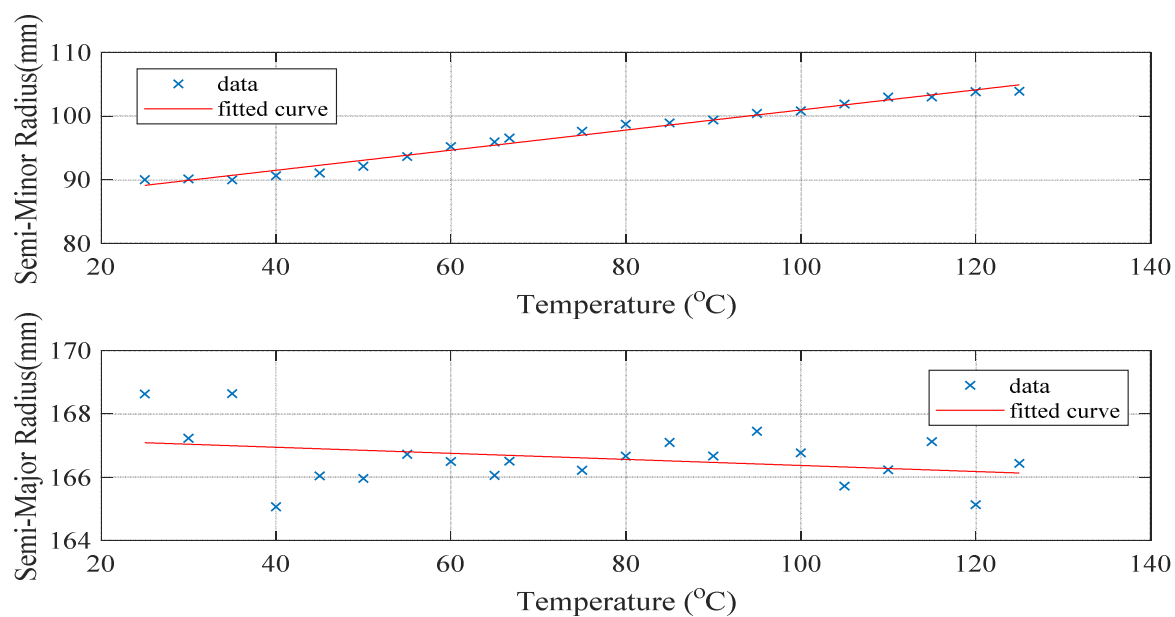


Figure 56. Benzoic Acid Inflatable: Estimated Semi-Major/Semi Minor Radius vs Temperature

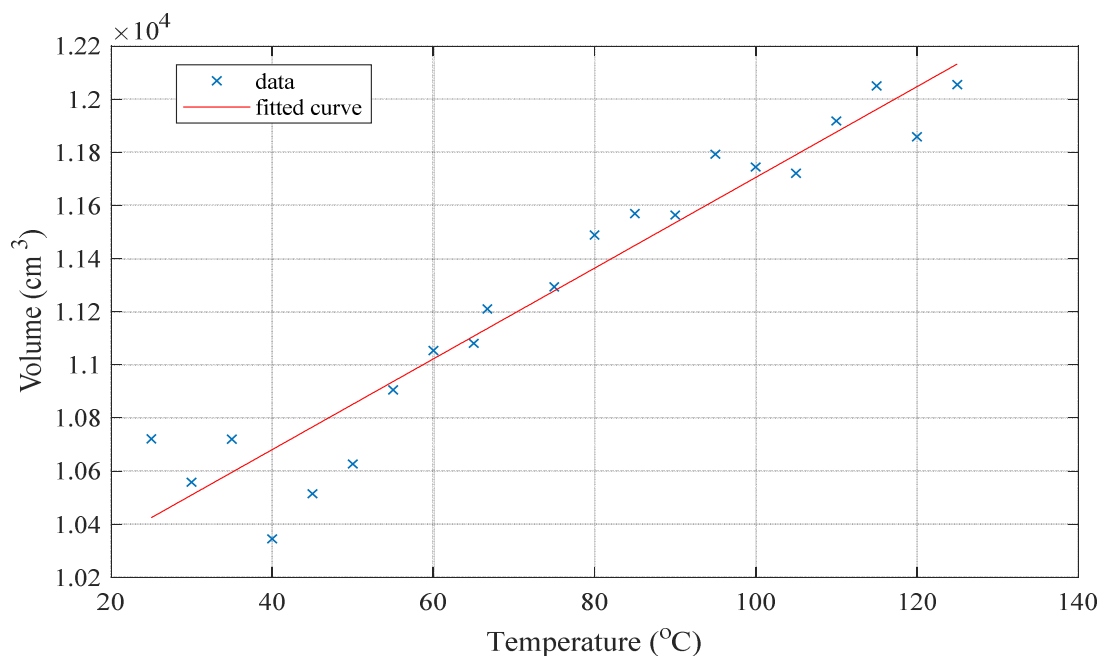


Figure 57. Benzoic Acid Inflatable: Estimated Volume vs. Temperature

## CHAPTER VII

### DISCUSSION

The analysis and tests performed in this thesis may provide an effective way of providing deorbit control investigated the viability of an inflatable CubeSat drag device that utilizes a sublimating inflation system. Estimations of the saturation vapor pressure provided approximations of the expected internal pressures of an inflatable as a function of temperature. From those estimates, passive inflation temperature requirements were established. Subsequently, an orbiting thermal model was developed to assess the passive inflation potential with respect to various 1000 km orbital inclinations.

In an effort to determine the pressure requirements needed to inflate the drag brake bladder, differential pressure tests were conducted relating imposed internal pressures to the geometric characteristics of the drag brake bladder. Results from the differential pressure tests showed an 0.5 torr minimal internal pressure requirement for inflating the drag brake bladder. Subtle changes in the shape of this bladder with changes in internal pressure were observed. In particular, variations were observed in the semi-major and semi-minor radii and resulting volume estimates of the inflatable bladder. It was shown that the 90% of the total inflatable volume was achieved with a differential pressure of 0.01 torr.

The thermal vacuum tests documented aspects of the functionality of the sublimating compound inflation system in a simulated space environment. The thermal vacuum test of the residual air inflatable was conducted in an effort to explore the possibility of utilizing a fully-stowed and folded drag brake bladder containing only residual air. Although somewhat

encouraging, this possibility must be carefully documented due to the dynamic behavior of residual air expansion and its potentially catastrophic behavior.

The exposure of the air test article in the vacuum conditions showed that a seemingly inconsequential quantity of air in the fabricated test articles resulted in a significant contribution to the overall inflation. At the end of the test, the air test article reached an estimated semi-major and semi minor radius of 165mm and 89mm respectively, and an estimated inflated volume of 10100 cm<sup>3</sup> at an ambient chamber pressure of 0.5 torr. The startling expansion ratio corresponds to the sensitivity of the results exploited in the differential pressure tests.

The significant air-derived expansion was similarly encountered during the thermal vacuum test of the benzoic acid inflatable. Despite these rather compromising air expansion results, the benzoic acid inflatable showed a measureable increase in semi-major and semi-minor radii and the resulting overall volume of the test article when subjected to the anticipated orbital temperatures.

At ambient chamber temperature, the benzoic acid inflatable auto-expanded to a volume of 10720 cm<sup>3</sup> during evacuation of the chamber. Once the chamber was fully evacuated, the temperature was ramped up to 125 °C and the benzoic acid inflatable expanded to an estimated volume of 12050 cm<sup>3</sup>. This volumetric expansion change exhibits a substantial increase in the internal pressure of the test article.

Condensed benzoic acid was observed on the inside surface of the top Mylar sheet following the test, as shown in Figure 59. The condensed powder collected around the fiducial dots show benzoic acid vapor sublimated and condensed non-uniformly inside the test article.



Figure 58: Benzoic Acid Inflatable Condensed Powder

Additionally, several “ribs” were observed on the surface of the test article, as shown in Figure 60. These ribs are a characteristic of the inflatable surface when the internal pressure is sufficiently high. Because the ribs were present following the test, they represent a sign of plastic deformation on the skin and a substantial internal pressure. These significant observations and results from the benzoic acid inflatable show that the subliming compound provided a reasonable and effective gas generator for inflation.



Figure 59. Benzoic Acid Inflatable Surface “Ribs”

Because the expansion of the residual air contributed a significant volume of gas in the overall inflation, future research needs to be conducted in the preparation and evacuation of the drag brake bladders. Although the internal pressure of the inflatable is small, auto-inflation can result in a potentially catastrophic inflation event. Prior to testing, the fabricated test articles were evacuated to 1 torr to limit the effects of auto-inflation. When both test articles were subjected to the vacuum conditions, the expansion of “inconsequential air” in both inflatables contributed towards a major fraction of to the overall inflation. Despite these results, the benzoic acid thermal vacuum test represented valuable data and observations in understanding the performance and effectiveness of a sublimating compound inflation system.

## CHAPTER VIII

### CONCLUSIONS

This thesis was conducted to determine the feasibility of deploying a low-cost, passively inflated drag brake for CubeSats to enable access to high orbital altitudes in compliance with the IADC 25-year lifetime constraint. Building from the NASA *Echo Satellite* project, the examined concept utilized subliming benzoic acid powder to inflate a folded and stowed bladder, thereby leading to a low-cost, miniaturized de-orbit system that can be integrated as part of a CubeSat chassis.

This study demonstrated theoretically and experimentally the practicality of a subliming compound inflation system. Static inflation and vacuum tests conducted in a large vacuum chamber at NASA LaRC demonstrated the minimal external absolute pressure required to fully inflate these bladder structures. However, the virtually undetectable volume of ambient residual air in the fabricated membrane bladders resulted in a significant contribution to the overall bladder inflation.

Although the final test articles were subjected to a one torr environment prior to the actual vacuum tests, it was not possible to evacuate all of the associated valves and fittings completely, thus resulting in significant air-derived expansion prior to sublimation during the controlled thermal vacuum tests. After additional research, it was learned that this residual air problem has been encountered frequently, sometimes resulting in catastrophic inflation. Despite these somewhat compromised experimental results, the thermal vacuum test for a test article bladder containing appropriate quantities of benzoic acid powder showed the functionality of a

subliming compound inflation system. Results from the benzoic acid inflatable vacuum test showed a measureable increase in internal pressure when the heated platen temperatures approximated the anticipated sun-side orbital temperatures.

This thesis has provided basic data demonstrating the feasibility of a deployable and passively inflated drag brake utilizing a subliming compound for inflation. Although the residual air presented problems with the premature expansion of the inflatable, the sublimating compound was shown to be a reasonable gas generator for inflation. Future work in limiting the auto-expansion due to residual air can optimize these systems in evolving a viable drag device to accelerate CubeSat orbital decay in compliance with the 25-year orbital lifetime limit at altitudes above 600 km.

### **Recommendations for Future Work**

There are several research recommendations for future progress of this concept:

1. A more reliable method is needed to limit the quantity of residual air remaining in a conventionally-manufactured bladder.
2. Deployment tests should be performed in a vacuum chamber to simulate the impulsive release of an auto-inflated drag brake.
3. An adequate drag brake structure rigidization technique should be validated in order to prove that the inflated structural shape can be maintained long after losing internal pressure as a result of micrometeorite bombardment.
4. A tether system for anchoring the drag brake to the CubeSat is required to maintain a stably-deployed drag brake for up to 25 years.

## REFERENCES

- [1] More, R.G., “The First Small Satellites: Sputnik, Explorer, and Vanguard”, in *Small Satellites: Past, Present, and Future*, edited by Helvajian, H., and Janson, S.W., The Aerospace Press, El Segundo, CA, 2008, Chapter 1, pp.1-46.
- [2] Wertz, J.R. , Larson, W.J., *Space Mission Analysis and Design*, Third Edition, Microcosm Press, Hawthorne, CA, 1999 Chapter 20, pp.802.
- [3] Richardson, G., Schmitt, K., Covert, M., Rogers, C., “Small Satellite Trends 2009-2013”, *29<sup>th</sup> AIAA/USU Conference on Small Satellites*, Logan, Utah, 2015.
- [4] Doncaster, B., Williams, C., Shulman, J., “2017 Nano/Microsatellite Market Forecast”, SpaceWorks Enterprises, Inc., Atlanta, GA, 2007.
- [5] Janson, S.W., “The History of Small Satellites”, in *Small Satellites: Past, Present and Future*, edited by Helvajian, H., and Janson, S.W., The Aerospace Press, El Segundo, CA, 2008, Chapter 2, pp. 47-88.
- [6] Anon, “Achieving Science with CubeSats: Thinking Inside the Box”, National Academies of Science Engineering and Medicine, Division on Engineering and Physical Sciences, Space Studies Board, Committee on Achieving Science Goals with CubeSats, The National Academies Press, Washington, DC, 2016
- [7] Anon, “Small Spacecraft Technology State of the Art”, NASA-TP-216648, 2015.
- [8] Ailor, W., Chobotov, V., Peterson, G., Patera, R., “Small Satellites: Debris and Reentry Hazards”, in *Small Satellites: Past, Present and Future*, edited by Helvajian, H., and Janson, S.W., The Aerospace Press, El Segundo, CA, 2008, Chapter 22, pp. 729.
- [9] Anon, “Handbook for Limiting Orbital Debris”, NASA-HDBK-8719.14, 2008.
- [10] Anon, “IADC Space Debris Mitigation Guidelines,” IADC-02-01, Inter-Agency Space Debris Coordination Committee, 15 October 2002.
- [11] Anon, “Space Systems – Determining Orbit Lifetime”, ISO/TC 20/SC 14 27852, ANSI Secretariat, International Organization for Standardization, 25 April 2007.
- [12] Ailor, W., Chobotov, V., Peterson, G., Patera, R., “Small Satellites: Debris and Reentry Hazards”, in *Small Satellites: Past, Present and Future*, edited by Helvajian, H., and Janson, S.W., The Aerospace Press, El Segundo, CA, 2008, Chapter 22, pp. 757-760.
- [13] Shmuel, B., “Canadian Advanced Nanospace Experiment 7 (CanX-7) Mission Analysis, Payload Design and Testing”, M.S. Thesis, Graduate Department of UTIAS, University of Toronto, 2012.
- [14] Nock, K.T., McDonald, A.D., Aaron, K.M., “Balloon Device for Lowing Space Object Orbits” U.S. Patent 6830222 B1, December 13, 2004.

- [15] Clemmons, D.L., “The Echo I Inflation System”, NASA TN D-2194, 1964.
- [16] Hansen, J.R., “The Odyssey of Project Echo”, *Space Flight Revolution*, NASA SP-4308, 1995.
- [17] Barham J., Jackson T., Lynch T., McNamara J., Powell J., Sokolsky A., Tarnacki T., Webb M., “CubeSat DeOrbit System Final Report MAE 435”, Mechanical and Aerospace Engineering Department, Old Dominion University, Norfolk, VA, 2014.
- [18] E. Lokcu, "Design Considerations for CubeSat Inflatable Deorbit Devices in Low Earth Orbit," M.S. thesis, Mechanical and Aerospace Engineering Department, Old Dominion University, Norfolk, VA, 2010.
- [19] Minzner, R. A., Champion, K. S. W., and Pond, H. L., “The ARDC Model Atmosphere, 1959”, Air Force Surveys in Geophysics No. 115, Air Force Cambridge Res. Center, 1959.
- [20] Lin, J.K.H., Sapna, G.H., Scarborough, S.E., Cadogan, D.P., “Inflatable Rigidizable Isogrid Boom Development”, ILC Dover, Inc., Frederica, DE, 2002.
- [21] Mladenov, I. M., Oprea, J., “The Mylar Balloon Revisited”, *The American Mathematical Monthly*, Pro Quest SciTech Collection, 2003.
- [22] Roark, R.J., Young, W.C., “Formulas for Stress and Strain Fifth Edition”, McGraw-Hill Book, Inc., New York, N.Y., 1975.
- [23] Yang, J.Y., Huang, J.C., “Rarefied Flow Computations Using Nonlinear Model Boltzmann Equations”, *Journal of Computational Physics*, Volume 120, Issue 2, 1995.
- [24] Moe, K., Moe, M.M., “Gas-Surface Interactions and Satellite Drag Coefficients”, *Planetary and Space Science*, Volume 53, Issue 8, 2005.
- [25] Pilinski, M.D., “Dynamic Gas-Surface Interaction Modeling for Satellite Aerodynamic Computations”, *Aerospace Engineering Sciences Graduate Theses & Dissertations*, Paper 37, University of Colorado at Boulder, 2011.
- [26] Schenk M., Viquerat, A.D., Seffen, K.A., Guest, S.D., “Review of Inflatable Booms for Deployable Space Structures: Packing and Rigidization”, *Journal of Spacecraft and Rockets*, Vol.51, No.3, University of Cambridge, 2014.
- [27] Moeller, C.R., “Design and Ground-Testing of an Inflatable-Rigidizable Structure Experiment in Preparation for Space Flight”, M.S. Thesis, Department of Aeronautics and Astronautics, Air Force Institute of Technology, 2005.
- [28] Frierse, G. J., Bilyeu, G.D., Thomas, M., “Initial ‘80s Development of Inflated Antennas”, L’Garde Inc., NASA-CR-166060, 1983.

- [29] The Chemical Company, <https://thechemco.com/chemical/benzoic-acid/>, March 2017.
- [30] Anon, "Benzoic Acid", NIST Chemistry WebBook, NIST Standard Reference Database Number 69, National Institute of Standards and Technology, Gaithersburg MD, 20899, March 2017.
- [31] Borgnakke, C., Sonntag, R.E., "Fundamentals of Thermodynamics Eighth Edition", *Properties of Pure Substances*, John Wiley & Sons, Ltd, Hoboken, NJ, 2013.
- [32] <http://antoine.frostburg.edu/cgi-bin/senese/searchglossary.cgi?query=clausius-Clapeyron+equation&nohead=yes&nofoot=yes>, March 2017.
- [33] Chatterjee, K., Dollimore, D., Alexander, K., "A New Application for the Antoine Equation in Formulation Development", College of Pharmacy and Department of Chemistry, The University of Toledo, Toledo, OH, 2001.
- [34] Borgnakke, C., Sonntag, R.E., "Fundamentals of Thermodynamics Eighth Edition", *Properties of Pure Substances*, John Wiley & Son Ltd, Hoboken, NJ, 2013.
- [35] <http://www.arknovin.com/en/quality-control/surface-quality/surface-roughness.html>, March 2017
- [36] Shapiro, I.I. and H.M. Jones, "Perturbations of the Orbit of the Echo Balloon," *Science*, Vol. 132, pp. 1484-1486, 1960.
- [37] Fortescue, P., Swinerd, G., Stark, J., "Spacecraft Systems Engineering Fourth Edition," John Wiley & Son Ltd, Hoboken, NJ, 2011.
- [38] VanOutryve, C.B., "A Thermal Analysis and Design Tool for Small Spacecraft," Master's Theses, San Jose State University, 2008.
- [39] Stevenson, J.A., Crafton, J.C., "Radiation Heat Transfer Analysis for Space Vehicles", Space and Information Systems Division North American Aviation Inc., Flight Accessories Laboratory, ASD Technical Report 61-119, 1961.
- [40] Bernal, W., "Relating Burst pressure to Seal Peel Strength in Pouches", M.S. Thesis, Clemson University, Clemson, SC, 2012
- [41] Landau, M.K., Choo, B.Y., Beling, P.A., "Simulating Kinect Infrared and Depth Images", *IEEE Transactions on Cybernetics*, Vol. 46, No. 12, December 2016.
- [42] Mallick, T., Das, P.P., Majumbar, A.K., "Characterization of Noise in Kinect Depth Images", *IEEE Sensors Journal*, Vol. 14, No. 6, June 2014.

- [43] Khoshelham, K., “Accuracy Analysis of Kinect Depth Data”, International Archives of the Photogrammetry, Remote Sensing and Spatial Information Sciences, Vol. 38, Calgary, Canada, August 2011
- [44] <https://www.mathworks.com/matlabcentral/fileexchange/24693-ellipsoid-fit?requestedDomain=www.mathworks.com>, March 2017.

## APPENDIX A

### SPACECRAFT'S POSITION VECTOR DETERMINATION

In order to determine a spacecraft's position vector, there are several coordinate systems in which an orbit that need to be defined. The geocentric-equatorial system has the origin at the center of the Earth with  $\hat{I}$  pointing in the vernal equinox direction,  $\hat{J}$  pointing in the sun line direction, and  $\hat{K}$  pointing towards the North Pole. This coordinate system is assumed as the inertial coordinate system.

The perifocal coordinate system lies inside the orbital plane and is assumed to be a fixed coordinate system. Unit vector  $\hat{i}$  lies in the direction of the periapsis point,  $\hat{k}$  lies normal to the orbital plane, and  $\hat{j}$  completes the right hand rule. The components of the position vector of a spacecraft in the perifocal system are:

$$\vec{R} = (r * \cos v)\hat{i} + (r * \sin v)\hat{j} \quad (25)$$

Where  $r$  is the magnitude of the position vector expressed as,  $r = \frac{p}{1+e \cos v}$ , and  $p$  is the semi-latus rectum given by  $p = a(1 - e^2)$ .

The position needs to be related in terms of the inertial (geocentric-equatorial) coordinate system. To transform the position vector from the perifocal coordinate system to the geocentric equatorial system, the following transformation matrix can be used.

$$C_{p2I} = \begin{bmatrix} \cos \Omega \cos \omega - \sin \Omega \cos i \sin \omega & -\cos \Omega \sin \omega - \sin \Omega \cos i \cos \omega & \sin \Omega \sin i \\ \sin \Omega \cos \omega + \cos \Omega \cos i \sin \omega & -\sin \Omega \sin \omega + \cos \Omega \cos i \cos \omega & -\cos \Omega \sin i \\ \sin i \sin \omega & \sin i \cos \omega & \cos i \end{bmatrix} \quad (26)$$

$$[\vec{R}]^I = [C_{p2I}] [\vec{R}]^p \quad (27)$$

Employing the matrix equation will transform the spacecraft's position vector from the perifocal coordinate system,  $[\vec{R}]^p$ , to the inertial coordinate system,  $[\vec{R}]^I$ .

## VITA

Adam Charles Horn

Old Dominion University  
Batten College of Engineering & Technology, Mechanical and Aerospace Engineering  
Department

### EDUCATION

Bachelor of Science, Mechanical Engineering, Old Dominion University, Norfolk, Virginia. May 2015.

### RESEARCH EXPERIENCE

Virginia CubeSat Constellation, Old Dominion University, Norfolk, Virginia. Provided guidance to the Virginia CubeSat Constellation USIP project undergraduate design teams. Advised and provided feedback on thermal analysis, structural design, prototyping, component selection, and integration and testing for CubeSat. Educated teams to systems engineering, subsystem modeling, mission requirements identification, development, planning and execution, and the design review process. January 2016/ August 2017.

RockSAT-C, Old Dominion University, Norfolk, Virginia. Designed and built a scientific payload on a Terrier Improved Orion to transmit flight data to the Old Dominion University Ground Station. Collected and analyzed atmospheric data and solar cell data, evolving around the use of a smartphone based flight system. Responsible for managing the mechanical team for two consecutive years, performing Finite Element Analysis on payload structure, conducting in house vibration testing, payload prototyping and integration, post-flight data analysis, and presenting design reviews. August 2014/ June 2016.

### PRESENTATIONS AT PROFESSIONAL MEETINGS

Horn, A., *A Low Cost Inflatable CubeSat Drag Brake Utilizing Sublimation*. Poster presentation at the 31<sup>st</sup> Annual AIAA/USU Conference on Small Satellites. Utah State University, Logan, Utah, August 2017

### PROFESSIONAL MEMBERSHIP

American Institute of Aeronautics and Astronautics  
American Society of Mechanical Engineers  
Society of American Military Engineers